



# A multi-model study of the restratification phase in an idealized convection basin

Clément Rousset<sup>a,\*</sup>, Marie-Noëlle Houssais<sup>a</sup>, Eric P. Chassignet<sup>b</sup>

<sup>a</sup> LOCEAN-IPSL, UMR 7159, Université Paris 6, Boîte 100, 4 Place Jussieu, 75005 Paris, France

<sup>b</sup> Center for Ocean-Atmospheric Prediction Studies, Florida State University, Tallahassee, FL, USA

## ARTICLE INFO

### Article history:

Received 1 November 2007

Received in revised form 15 July 2008

Accepted 31 August 2008

Available online 11 September 2008

### Keywords:

Baroclinic instability

Convection basin

Model intercomparison

Restratification

Eddies

Idealized simulations

## ABSTRACT

The representation of baroclinic instability in numerical models depends strongly upon the model physics and significant differences may be found depending on the vertical discretization of the governing dynamical equations. This dependency is explored in the context of the restratification of an idealized convective basin with no external forcing. A comparison is made between an isopycnic model including a mixed layer (the Miami Isopycnic Coordinate Ocean Model, MICOM), its adiabatic version (MICOM-ADIAB) in which the mixed layer physics are removed and the convective layer is described by a deep adiabatic layer outcropping at the surface instead of a thick dense mixed layer, and a z-coordinate model (OPA model).

In the absence of a buoyancy source at the surface, the mixed layer geometry in MICOM prevents almost any retreat of this layer. As a result, lateral heat exchanges in the upper layers are limited while mass transfers across the outer boundary of the deep convective mixed layer result in an unrealistic outward spreading of this layer. Such a widespread deep mixed layer maintains a low level of baroclinic instability, and therefore limits lateral heat exchanges in the upper layers over most of the model domain. The behavior of the adiabatic isopycnic model and z-coordinate model is by far more satisfactory although contrasted features can be observed between the two simulations. In MICOM-ADIAB, the more baroclinic dynamics introduce a stronger contrast between the surface and the dense waters in the eddy kinetic energy and heat flux distributions. Better preservation of the density contrasts around the dense water patch maintains more persistent baroclinic instability, essentially associated with the process of dense water spreading. The OPA simulation shows a faster growth of the eddy kinetic energy in the early stages of the restratification which is attributed to more efficient baroclinic instability and leads to the most rapid buoyancy restoring in the convective area among the three simulations. Dense water spreading and warm surface capping occur on fairly similar time scales in MICOM-ADIAB although the former is more persistent than the latter. In this model, heat is mainly transported by anticyclonic eddies in the dense layer while both cyclonic and anticyclonic eddies are involved in the upper layers. In OPA, heat is mainly brought into the convective zone through the export of cold water trapped in cyclonic eddies with a strong barotropic structure. Probably the most interesting difference between the z-coordinate and the adiabatic isopycnic model is found in the temperature distribution ultimately produced by the restratification process. OPA generates a spurious volume of intermediate water which is not seen in MICOM-ADIAB where the volume of the dense water is preserved.

© 2008 Elsevier Ltd. All rights reserved.

## 1. Introduction

A large part of the deep water masses of the world ocean are formed in semi-enclosed basins (the Labrador Sea, the Greenland Sea, or the Mediterranean Sea). Observations and numerical simulations conducted in these regions show that the convection can be divided into three phases: a preconditioning phase during which the cyclonic gyre-scale circulation rises isopycnals at the centre of the gyre, bringing the weakly stratified deep water close to the surface, which then appears as a thick homogeneous dense water

lens underneath the relatively thin stratified surface layer; a mixing phase initiated by intense surface cooling which erodes the stratified surface water and, for a large enough buoyancy loss, makes it overturn in several plumes and rapidly mix to form a deep homogeneous convective patch; a restratification phase during which a new stratified water column occupying the upper and intermediate layers of the convective patch is established.

Two mechanisms contribute to the restratification, buoyancy added to the surface through heating from the atmosphere or sea ice melt water release, and lateral advection of buoyant stratified water from the periphery of the convective patch. When the mean circulation follows predominantly a circular path around the convective region, lateral exchange must occur primarily via

\* Corresponding author. Tel.: +33 1 44 27 70 71; fax: +33 1 44 27 38 05.

E-mail address: [clement.rousset@locean-ipsl.upmc.fr](mailto:clement.rousset@locean-ipsl.upmc.fr) (C. Rousset).

mesoscale eddies generated through baroclinic instability of the mean flow (Morawitz et al., 1996). The process is efficient if a buoyant reservoir can be maintained at the periphery of the convective zone through, e.g., a warm boundary current (Lilly et al., 1999). After being restratified, the convective basin is capped by a light surface layer overlying a thick lens of dense homogeneous water, which is a remnant of the previous mixing event. The resulting stratification, especially the characteristics and the thickness of the upper stratified layer, depends upon the efficiency of the restratification processes and ultimately determines the ability of the water column to be destabilized upon entering a new convection cycle.

The dynamics of the convection patch controls the restratification process. The instability builds on the potential energy stored in the front separating the outcropping dense, homogeneous water from the surrounding stratified waters, and, to a lesser extent, on the large scale kinetic energy associated with the rim current in thermal wind balance with this front. Deformation of the mean cyclonic circulation pattern rapidly occurs in which the energy of the large scale flow cascades to smaller scale perturbations. If the radius of the mixed patch is greater than the Rossby deformation radius, the patch is baroclinically unstable and the potential energy of the perturbations is converted into kinetic energy (Marshall and Schott, 1999). Barotropic instability may also occur, in relation to the horizontal shear of the rim current. Several eddies are formed which transport buoyant water from the surroundings to the interior of the convective patch whereas the cold dense water is exported from the convective patch towards the periphery. The role of the eddy fluxes in the restratification has been partially documented by observations in the different convective regions of the world ocean. These suggest that eddy fluxes alone could explain the restratification without the need for an additional buoyancy input from the atmosphere (Send et al., 1995; Lilly et al., 2003). From data collected in the 1990s, Lilly et al. (2003) estimated the eddy contribution to the lateral heat exchange between the boundary and the interior of the Labrador Sea to about 25%.

Analytical considerations together with numerical simulations and laboratory experiments have also demonstrated the central role of geostrophic eddies associated with the baroclinic instability of the rim current in controlling the restratification (Jones and Marshall, 1997). Eddies are believed to constrain the restratification time scale as well as the characteristics of the end products and, provided the restratification operates during the mixing phase, the depth of the convective layer (Visbeck et al., 1996). Smaller scale ageostrophic instabilities, known as mixed layer instabilities, occurring in the less stratified interior region of the mixed patch are also believed to contribute to the restratification, yet their existence is subject to the presence of spatial heterogeneities in the ML density distribution (e.g., Boccaletti et al., 2007). A key issue when addressing the restratification of a convective basin is to understand the link between the eddy heat fluxes and the eddy kinetic energy distribution. Dedicated experiments using more realistic configurations are needed in order to estimate these fluxes and better quantify their impact on the stratification of the basin in relation to the different model physics.

The representation of flow properties and the associated eddy field in numerical models is much dependent upon the model physics and most notably on the parameterization of the sub-grid-scale processes (e.g., Willebrand et al., 2001). In particular, major differences are seen when different vertical coordinates are used to discretize the governing dynamical equations. In the ocean interior, far from regions of high mixing rates, transport and mixing preferentially occur along isopycnal surfaces while diapycnal mixing remains fairly low (Griffies et al., 2000a). This high ratio ( $\sim 10^8$ ) of isopycnal mixing to diapycnal mixing is essentially guaranteed in isopycnal models where the two-dimensional trans-

port equation is consistent with the adiabatic framework. As a consequence, such models are well known to better perform in tracking water masses. By contrast, in z-coordinate models, the advection schemes only guarantee numerical convergence to approximate adiabaticity and numerical truncation errors and horizontal diffusion introduce spurious diapycnal mixing which unphysically alters the characteristics of the advected water masses (Griffies et al., 2000b). The problem is particularly critical in eddy resolving models where a relatively high horizontal resolution, compared to what would be requested to simulate a realistic eddy field and to dissipate the accumulated variance and enstrophy at the cut-off grid scale, appears to be necessary in order to reduce the level of spurious mixing to small acceptable values (Griffies et al., 2000b).

Stability analyses of a jet like stream have shown that the different representations of advection and mixing between isopycnal and z-coordinate models also have important consequences for the characteristics of the hydrodynamic instabilities. In the early stage of the instability of a jet like stream, dissipation is expected to reduce the growth rate of the instability. In z-coordinate models, spurious horizontal mixing of density occurring across the jet front tends to reduce the instability growth rate as sharp horizontal density gradients can hardly be sustained (Griffiths et al., 2000). On the other hand, implicit diffusion inherent to the transport scheme used in the continuity equation of the isopycnal models may be very large in weakly unstable flows, thus retarding the instability growth (Griffiths et al., 2000). In the non-linear phase of the instability, spurious diapycnal mixing has been shown to be responsible for retarding the eddy cut-off process in a two-layer z-coordinate model, leading to an overshoot effect on the eddy heat flux as the typical size of breaking waves tends to increase with increasing dissipation (Drijfhout, 1992).

In z-coordinate models, the effect of dissipation on the instability growth may be counteracted by effects of spurious potential vorticity gradients generated across the Rossby wave front. Such gradients which are the result of the non-potential-vorticity-conserving advection scheme tend to artificially enhance the wave growth (Drijfhout, 1992). Inadequate vertical discretization of the density field have the same effect (Ikeda and Wood, 1993) while vertical truncation errors in the advection scheme tend to shorten the wavelength of the fastest growing wave in the linear stage of the instability (Griffiths et al., 2000). These errors may also be responsible for a decrease of the mean kinetic energy and associated baroclinicity, and consequently of the barotropic and baroclinic instabilities (Bleck and Boudra, 1986). One should however remind that, due to the coarse vertical resolution of the models, most of the studies focusing on the impact of the vertical discretization often overestimate this impact.

The relative effects of diffusivity and viscosity on the baroclinic stability of the flow need to be clarified as they largely depend on the model set-up. While both viscosity and diffusivity dampen the wave growth, viscosity appears to influence the wavelength of the fastest growing wave more than diffusivity in the early stage of the instability (Griffiths et al., 2000). As stated by these authors, this result may be dependent on the particular choice of diffusion parameterization. Additionally, while for small dissipation viscosity largely controls the small scale potential vorticity, for larger dissipation diffusivity is expected to primarily influence the large scale vortex stretching and the conversion of available potential energy (Drijfhout, 1992). The relative impact on the heat transport is however difficult to assess due to the non-linear interactions between viscosity and diffusivity effects. One particular aspect to be clarified is the different effects of viscosity and diffusivity on the production and dissipation of the eddy kinetic energy.

Although isopycnal models are expected to perform better in an adiabatic fluid, the isopycnal representation is penalized in

case of thick homogeneous layers such as deep convective mixed layers. In such cases, the model vertical discretization in the upper water column becomes insufficient to properly represent vertical contrasts, in particular current shears associated with density fronts (Eldevik, 2002). An example of such a limitation is found in the time evolution of the stratification in the Labrador Sea as simulated by the Miami Isopycnic Coordinate Ocean Model (MICOM) (Fig. 1). After the end of the convective period (Fig. 1a), the deep mixed layer (ML) is subject to rapid retreat. The retreat starts in mid-April (Fig. 1b) through a one-dimensional rearrangement of the water properties (Fig. 1c) which, in this model, is essentially controlled by local heat and potential energy conservation requirements. At that time the retreat is not related to a surface capping by surrounding lighter waters but rather to surface warming. A light surface layer that leaves a homogeneous 500 m thick intermediate layer underneath is not restored before the end of April. Additionally, by June, when the restratification has been completed, the volume of the dense water trapped underneath the upper stratified layers is larger than the volume initially available in the ML at the end of the convective period (compare Fig. 1a and d). In contrast, observations at OWS Bravo during the same period show a gradual restratification of the intermediate water column until a rapid capping of the convected waters occurs by end of April (Fig. 2). Concomitantly, the light surface layer experiences a salinity decrease (Fig. 2b, bottom) which must have been triggered by advective processes. These observations suggest that the ML retreat in response to the surface buoyancy input from the atmosphere is not the primary mechanism involved in the seasonal restratification of a convective basin. Lateral buoyancy exchange with the surroundings of the homogeneous region is a more probable mechanism which needs to be properly represented in models.

In order to investigate the impact of different model physics on the dynamics of the restratification in a convective basin, a typical case study has been implemented based on three different models: a  $z$ -coordinate model, an isopycnic coordinate model including a mixed layer, and a purely isopycnic model in which the surface layer is treated as an adiabatic layer in the same way as the other model layers. The three simulations rely on a common experimental set-up (same initial stratification, no surface forcing). Our analysis focuses on relating the differences observed between the model simulations to the different representations of the meso-scale activity.

In Section 2, a brief description of each of the three models is given including a discussion of selected physical parameters. In Section 3, the models results are analyzed with a particular focus on comparing the kinetics and the efficiency of the restratification between the three models. In particular, diagnostics of the eddy activity in relation to instabilities are presented for the three models. A discussion follows in Section 4 and a summary is finally given in Section 5.

## 2. Numerical experiments

### 2.1. Model physics

Three models are compared which all solve the three-dimensional hydrostatic primitive equations on a staggered horizontal C-grid with no-slip conditions at the solid boundaries. All models are run with constant salinity. The primary difference between models is in the representation of the “vertical” coordinate. One of the models is a  $z$ -coordinate model (the OPA model, Madec et al., 1998) which, for the present analysis, includes a free surface on top. The stratification evolves through an advection-diffusion equation for the temperature (and, in the general case, the salin-

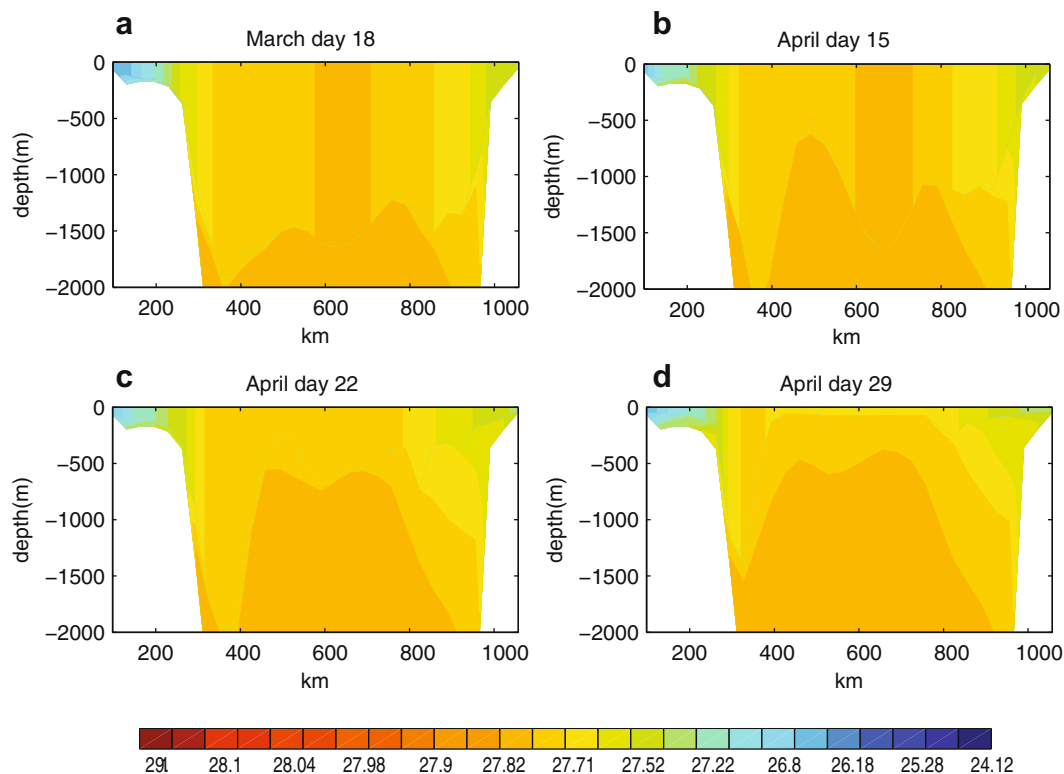


**Fig. 1.** Potential density (in  $\rho-1000 \text{ kg m}^{-3}$ ) distribution on the AR7W section in the Labrador Sea in 1972, as simulated by a MICOM experiment using realistic NCEP forcing (courtesy of J. Deshayes).

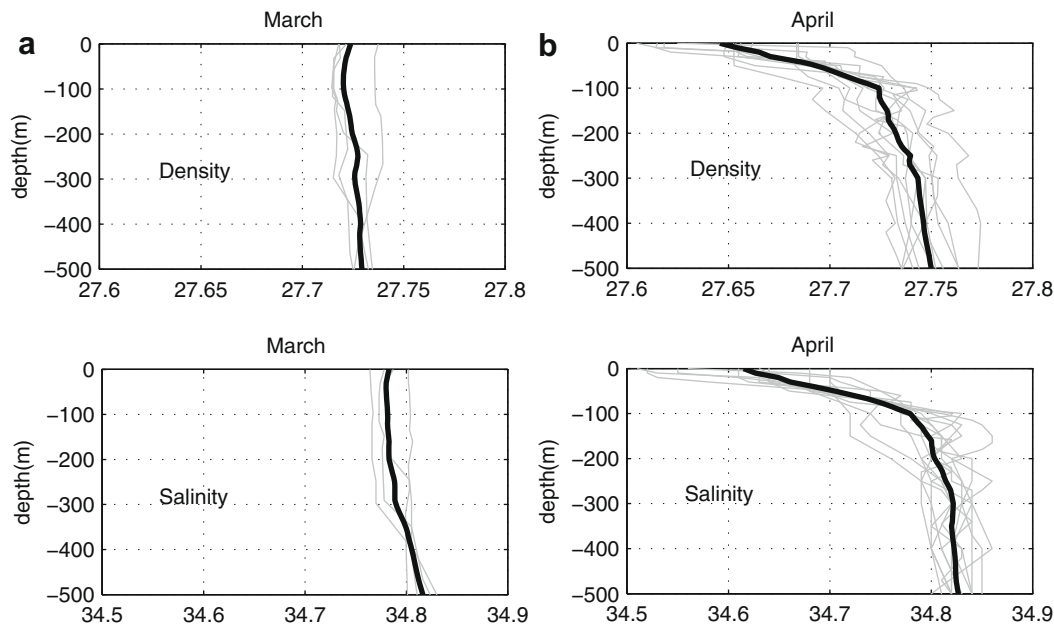


**Fig. 2.** Vertical distribution of potential density (in  $\rho-1000 \text{ kg m}^{-3}$ , top panels) and salinity (in pss, bottom panels) at OWS Bravo at the end of (a) March and (b) April. Thick black lines are the averaged profiles.

ity). Advection is treated with a second order centred-difference scheme. Viscous and diffusion processes are parameterized by second order diffusive operators with constant diffusion coefficients. A non-penetrative convective adjustment scheme takes care of the hydrostatic instability.

The second model, the Miami Isopycnic Coordinate Ocean Model (MICOM 2.8, e.g., Bleck et al., 1992) is an isopycnic layer model capped by a vertically homogeneous non-isopycnic (i.e., density varying) ML which takes care of diabatic surface exchanges with the atmosphere (Bleck et al., 1989). The evolution of the thickness and hydrographic properties of the ML as a result of vertical mixing is predicted by an entrainment equation based on the Kraus and Turner (1967) formulation. Underneath the ML, the vertical stratification is described by discrete homogeneous isopycnic layers. There is no friction at the layer interfaces and interaction between layers only occurs through hydrostatically transmitted pressure torques. The stratification evolves due to changes in the individual layer thicknesses described by the continuity equation. Advection and diffusion of momentum and tracers occur along isopycnals. In our particular case study, the salinity is held constant. There is no mass transfer across isopycnals in the interior, except when prescribed (weak background in the experiments described in this paper). Mass transfers can occur between the ML and the underlying layers which are associated with the removal of hydrostatic instabilities arising at the base of the ML as a result of changes in the ML properties. Within the ML, advection and diffusion of temperature and momentum are purely horizontal. Subgrid-scale mixing is parameterized by second order diffusive operators. A constant diffusivity is assumed for scalar properties while, for momentum, a deformation dependent viscosity (Smagorinsky, 1963) is used.

Our comparative analysis includes a third model which has been designed to investigate the impact of the ML physics. This model (referred to as MICOM-ADIAB) is a “purely isopycnic” version of the MICOM model in which the ML physics are turned off and the surface layer is treated as a constant potential density layer in the same way as the underlying layers. In this particular version, except for a weak prescribed diapycnal flux, the mass of all individual layers are conserved.

## 2.2. Experimental set-up

Three experiments using the three different models described above have been performed. All experiments are run with the same model domain and initial conditions with no external forcing. The domain consists of a flat bottom, circular basin of depth  $H_b = 1000 \text{ m}$  and diameter  $500 \text{ km}$  (Fig. 3a). The Coriolis parameter is constant and set to  $f_0 = 10^{-4} \text{ s}^{-1}$ . Salinity is maintained at a constant uniform value of  $34.9 \text{ pss}$  and the ocean density  $\rho$  only depends on temperature  $T$ . An equation of state is used in which the density is linearized around the initial bottom temperature using a thermal expansion coefficient of  $1.95 \cdot 10^{-4} \text{ }^\circ\text{C}^{-1}$ . For convenience, in the following, the model stratification will be described based on the temperature distribution.

The initial stratification is representative of conditions encountered at the end of a convective period in a subpolar convective basin (Fig. 3b). A typical Labrador Sea stratification has been selected. At the centre of the basin, a vertically homogeneous cylinder of radius  $R_c = 70 \text{ km}$ , filled with dense water of equivalent temperature  $T = 4.86 \text{ }^\circ\text{C}$ , extends from the surface down to  $H_c = 580 \text{ m}$  (Fig. 3a and b). This convective region is separated from a stratified domain by a  $30 \text{ km}$  wide front across which the temperature varies linearly. Over the rest of the model domain, the vertical stratification is described by a horizontally uniform density profile corresponding to a constant buoyancy frequency  $N = 1.9 \cdot 10^{-3} \text{ s}^{-1}$ . This stratification is representative of that encountered in the Labrador Sea boundary current if one excludes the very light Polar Surface Water (see, e.g., the AR7W sections in Pickart and Spall, 2007). The horizontal density gradient at the rim of the convective patch is also consistent with conditions encountered in the region. One should however notice that, since the salinity is held constant in our experiments, the temperature distribution cannot match the corresponding observed distribution. All models have 12 layers of thickness  $h_0 = 83.33 \text{ m}$  which are equally spaced at the beginning of the experiment in all three models. The convective patch initially extends over the upper seven model levels in OPA or, alternatively in MICOM (resp. MICOM-ADIAB) is entirely contained in the ML (resp. the 7th layer) of the model. It is important to note that in the particular experimental set-up used here, there is no mechan-

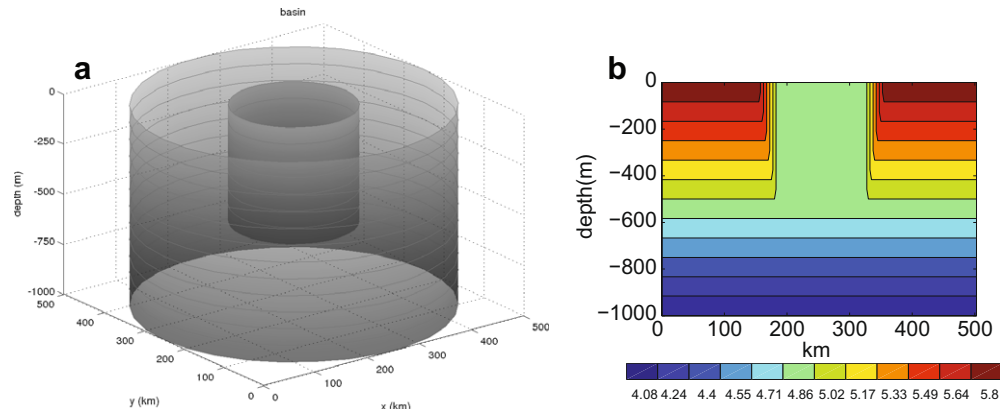


**Fig. 3.** Model configuration. (a) The model domain is a cylinder of radius  $R = 250$  km and depth  $H_b = 1000$  m. (b) The initial stratification is described by 12 equally spaced layers which are uniformly distributed over the whole model domain except in a central region of radius  $R_c = 70$  km and depth  $H_c = 580$  m where the stratification is homogeneous (see explanation in text).

ical or buoyancy source of turbulent energy at the surface and ML entrainment or retreat just cannot occur.

All models have the same horizontal resolution of 2.5 km which makes them eddy resolving in the more stratified water around the convective patch where the Rossby deformation radius,  $L_d = \frac{NH_c}{f_0}$ , is on the order of 10 km. In this definition of  $L_d$ , the depth of the convective patch  $H_c$  (rather than the total water column depth) is used, as the dynamical region is assumed to be concentrated along the density front, which mainly extends from the surface down to  $H_c$ .

Small values of the horizontal thermal diffusivity and viscosity ( $7.5 \text{ m}^2 \text{ s}^{-1}$ ) are chosen so that the diffusion time scale across the basin (order of years) is large compared to the typical restratification time scale (order of days). Still, in the isopycnic models, the Smagorinsky scheme may be responsible for locally larger values of the viscosity. Vertical diffusion in OPA and diapycnal diffusion in the isopycnic models both amount to  $10^{-5} \text{ m}^2 \text{ s}^{-1}$ . Diagnoses (not shown) of the respective contributions of diffusion and advection to the evolution of the temperature field show the strong predominance of the advection (both horizontal and vertical in OPA) over diffusion in all models. Diffusion is the largest in the frontal region at the rim of the convective patch where the isopycnals are steep and the horizontal temperature gradient strong. It contributes to about 10% of the three-dimensional heat exchanges in both OPA and MICOM-ADIAB but is dominated by the horizontal component in OPA and by the isopycnal fluxes in MICOM-ADIAB.

### 3. Results

#### 3.1. Evolution of the 3D temperature field

The analysis presented here focuses on the first months of the simulation, when the restratification process is the most active. Except for MICOM, the last panels (day 100) in Fig. 4 show a state of nearly complete restratification after the dense water has spread from the centre out to the periphery of the basin, reforming a fairly uniform dense layer. Noticeable differences are however seen in the vertical and horizontal distributions between the three models (Figs. 4 and 5). In MICOM-ADIAB (Fig. 4a), the surface of the convective patch is capped by a thin layer of warm water with similar properties as water at the periphery. This surface capping does not reach the centre of the basin until day 30 and an intermediate restratification is not effective before day 45. In Fig. 5a, the meanders in the upper layers (top panel) occur on scales much larger than  $L_d$  and are likely to be destabilized through baroclinic instability of the front separating the dense water patch from the sur-

roundings. The width of the front initially scales with three times the deformation radius characterizing the outer stratified region of the front, enabling a mixed barotropic/baroclinic (although soon to be predominantly baroclinic) instability. The lateral temperature gradient being the strongest in the uppermost layers, the capping of the convective region occurs primarily at the surface. Fig. 4a also shows the persistence of a dense homogeneous water lens on day 100 which is the remnant of the initial dense water patch.

In OPA, the restratification is slightly faster than in MICOM-ADIAB (Fig. 4c). On day 20, surface capping has already reached the centre of the domain and the intermediate restratification starts right afterwards. On day 100, contrasting with MICOM-ADIAB, the stratification of the basin is nearly uniform throughout the basin and the signature of the homogeneous dense water lens has almost disappeared. Intermediate waters are created to the detriment of the dense water. Meanders and eddies in Fig. 5c have scales comparable to those in MICOM-ADIAB but their domain of influence at depth extends further outward, consistent with the more efficient exchange in the intermediate layers.

In MICOM, neither the rapid surface capping by a thin warm layer nor a remnant convective layer underneath the surface layer are observed (Fig. 4b). The convective patch is only slowly eroded from the sides by the surrounding warmer waters, leaving a still deep homogeneous water column at the centre of the basin after 100 days. On day 180 (not shown), this homogeneous patch is slightly lighter but the restratification is still incomplete. Moreover, as the dense homogeneous patch laterally mixes with the surrounding intermediate layers, additional water incorporated into the ML leads to some ML deepening both in the centre and at the periphery of the patch. The meanders observed in the upper temperature field (Fig. 5b) are associated with smaller horizontal scales and narrower lateral temperature gradients than in MICOM-ADIAB.

An important limitation of the MICOM model is the impossibility of ML retreat in absence of a buoyancy input from the atmosphere which, in the real world, would drive part of the restratification in the convective region. The resulting reformation of a seasonal ML would then limit the vertical range over which the oversimplified homogeneous dynamics of the upper layer can be active. In the present MICOM experiment, lateral buoyancy exchange with the surrounding waters occurs uniformly over the entire depth range of the convective layer without the surface intensification needed for an efficient surface capping. In order to mimic a surface induced ML retreat, a sensitivity experiment has been performed, in which the MICOM model is initialized with the same density stratification as the standard one, but

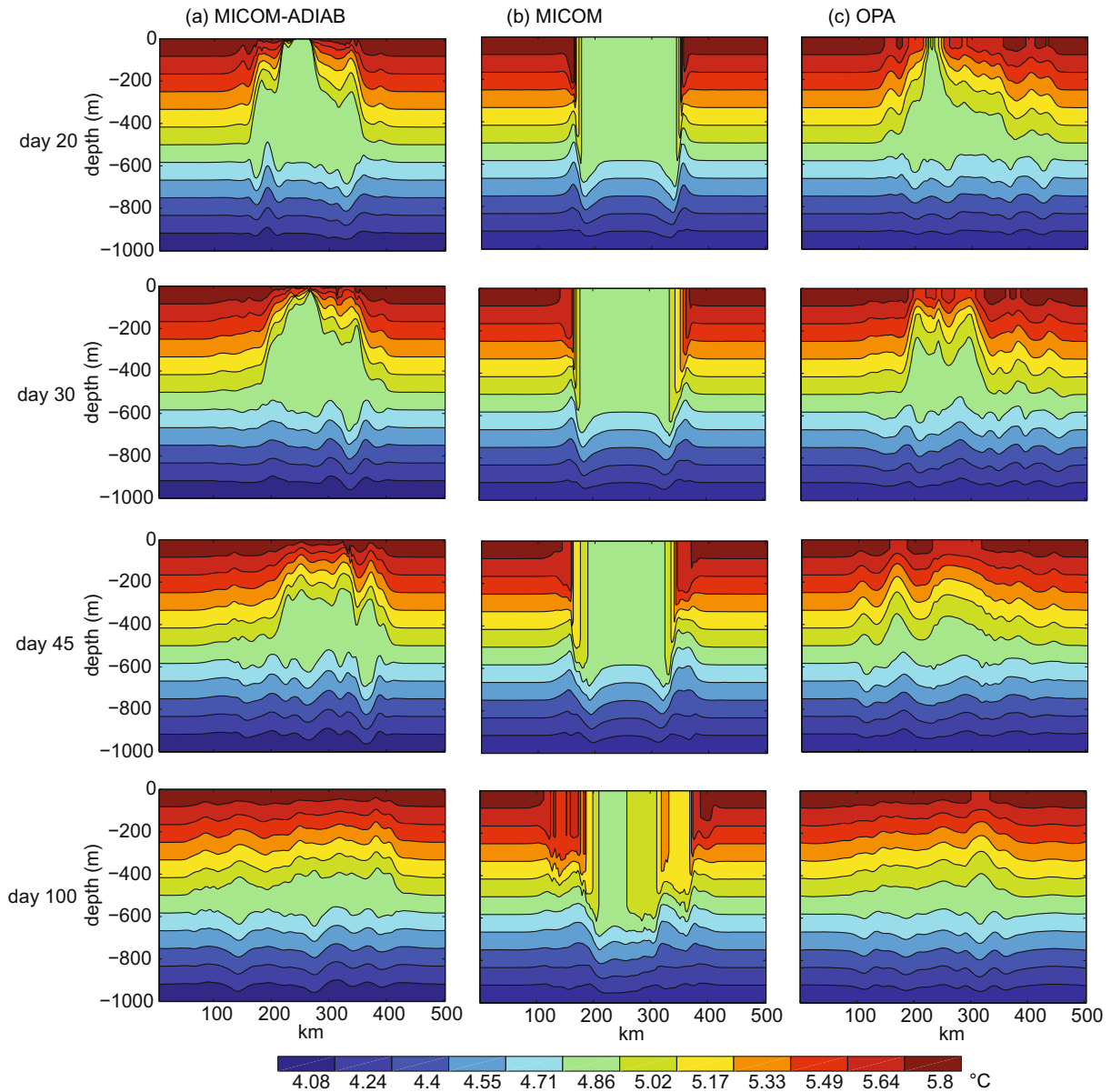


**Fig. 4.** Vertical temperature distribution (in °C) on a section through the centre of the basin at selected times of the integration for (a) MICOM-ADIAB, (b) MICOM, (c) OPA.

the initial ML depth is arbitrarily assumed to be uniformly equal to  $h_0 = 83$  m throughout the whole model domain including the convective patch. While the initial buoyancy of the water column is kept unchanged, the thin initial ML leaves below it the most of the convected water. As a consequence, this water now occupies an isopycnic layer which will conserve its volume throughout the restratification process. The preservation of the dense water volume and properties is essentially what one would expect to happen once the light surface layer has capped the dense water patch. The experiment, however, is not entirely convincing as the lateral heat exchanges within the ML still induce some deepening of this layer in the vicinity of the temperature front. This deepening signal is propagated outward so that after a year, a 300 m deep ML covers most of the basin. Moreover, while the ML characteristics in the centre of the basin are closer to the upper layer characteristics in the OPA or MICOM-ADIAB simulations, the ML is still too dense (temperature of 5.3 °C instead of 5.8 °C in MICOM-ADIAB). Buoyancy added to the surface layer would fix part of the problem.

### 3.2. Time evolution of the buoyancy in the convective patch

The kinetics of the restratification in the different models can be estimated from the time evolution of the buoyancy of the convective patch. This evolution captures altogether the effects of the upper layer restratification and of the dense water spreading away from the centre of the basin. The buoyancy of the convective patch is calculated over a fixed volume cylinder with same lateral extent as the initial homogeneous cylinder and extending down to the bottom to accommodate the different geometry of the layers in the isopycnic and z-coordinate models:

$$B(t) = \frac{1}{V} \int_V \int \int (-\rho g) dV \quad (1)$$

In (1), the integration is performed over the volume  $V$  of a cylinder of radius  $R_{lim} = 90$  km:  $V = \pi R_{lim}^2 H_b \sim 25 \times 10^3$  km<sup>3</sup>,  $g$  is the gravity and  $t$  is time. The limit of 90 km corresponds to the outermost location of the maximum of the eddy heat fluxes (see Section 3.5).

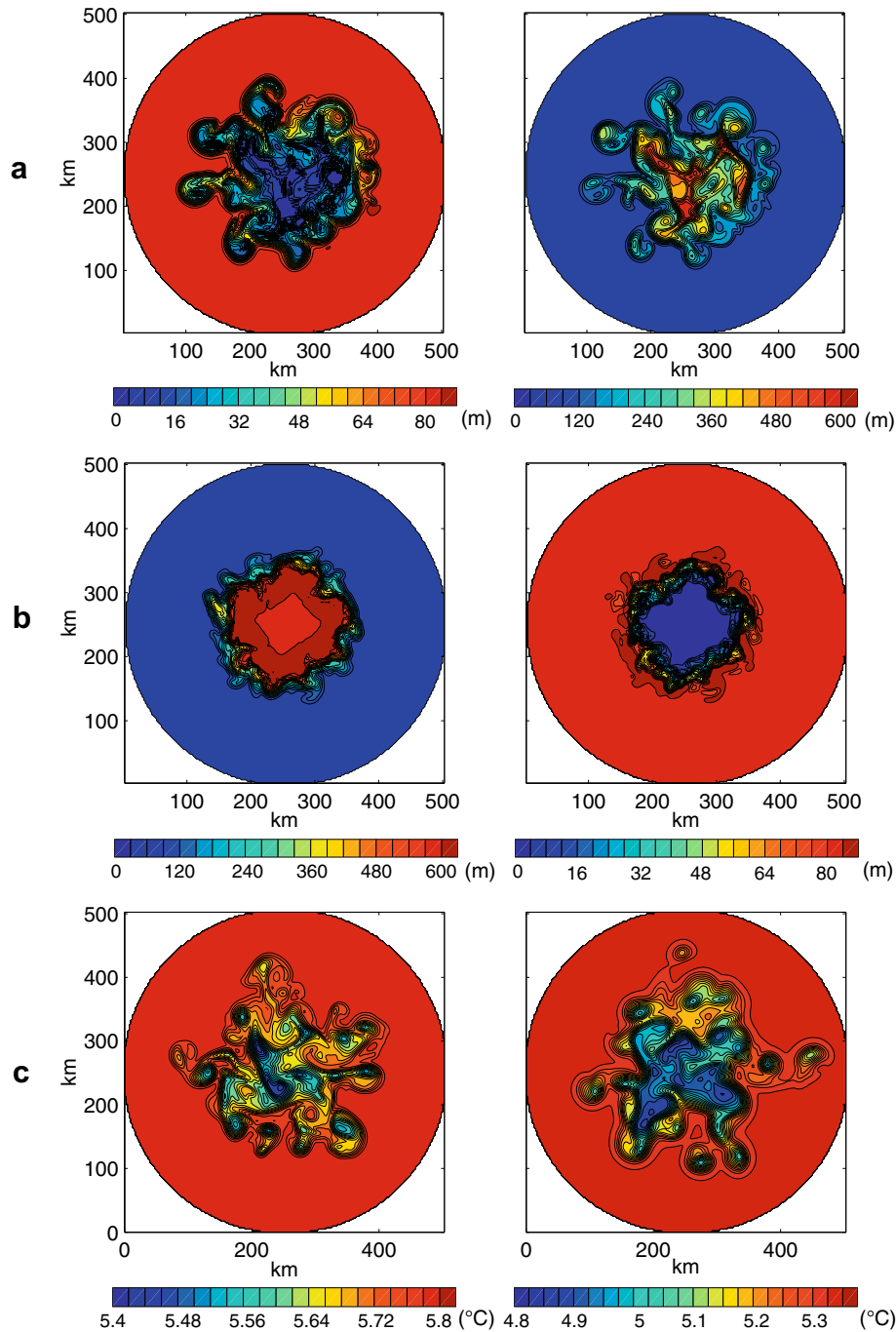


**Fig. 5.** Distribution of the upper (layer 1, left panels) and deep (layer 7, right panels) layer thickness (in m) in (a) MICOM-ADIAB, (b) MICOM, (c) distribution of temperature (in °C) at 40 m (left panel) and 290 m (right panel) in OPA. Horizontal distributions are shown as 3 day-averages around day 30. Note that in MICOM, the uppermost layer is the ML and initially contains the dense water volume.

In MICOM, a restratification time scale is difficult to estimate from the relative buoyancy change,  $\frac{B(t)-B(0)}{B(0)}$  (Fig. 6) as the buoyancy of the convective patch is still evolving after a year, indicating incomplete restratification. The timing of the restratification is not very different between OPA and MICOM-ADIAB although the restratification occurs slightly faster in the former simulation, with a characteristic time scale of 70 days compared to 80 days. This is in agreement with the qualitative conclusion drawn from Fig. 4.

Since all experiments are unforced, the ultimate buoyancy characterizing the restratified convective patch on day 100 (Fig. 4) is an indicator of the efficiency of the lateral eddy heat fluxes. Similar

buoyancies are found in OPA and MICOM-ADIAB which suggest similar convergence of the heat transport into the convective zone. In MICOM, lateral advection across the density front at the outer boundary of the deep ML is probably not as efficient to transfer heat from the outer part of the domain into the interior, leading to much lower final buoyancy. The predominant role of the mixed layer is also evidenced in the “imposed ML retreat” simulation. Prescribing an initially shallow ML slightly improves the early stages of the simulation but, as in the standard MICOM simulation, the buoyancy does not stabilize and remains fairly low compared with the other two models.

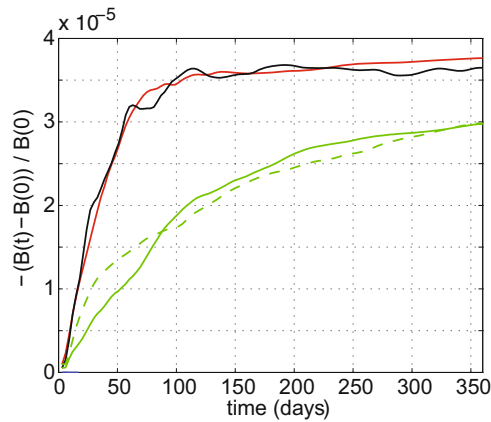


**Fig. 6.** Time evolution of the relative change of buoyancy  $\frac{B(t)-B(0)}{B(0)}$  integrated over the whole water column in the central part (cylinder of radius 90 km) of the domain for MICOM-ADIAB (red), MICOM (green), and OPA (black). The additional dashed green curve represents the “imposed-retreat” experiment. (For interpretation of colour mentioned in this figure the reader is referred to the web version of the article.)

The above differences between OPA and MICOM-ADIAB are likely to be related to differences in the heat advection schemes but perhaps also to the different levels of instability of the rim current. This level can be estimated from the restratification time scale,  $\tau_{\text{restrat}}$ , as given by Jones and Marshall (1997) theoretical expression which, once reformulated for the case of a front wider than the deformation radius (Katsman et al., 2004), takes the form:

$$\tau_{\text{restrat}} = \frac{3}{2c_e} \frac{L_f R_c}{L_d N H_c} \quad (2)$$

in which  $L_f$  is the front width (here equal to 30 km) and  $c_e$  is a constant measuring the efficiency of the eddy transfers across the front. The associated values of  $c_e$  are 0.040 in MICOM-ADIAB and 0.047 in OPA. Both values are very close to the theoretical value of 0.045 deduced by Spall and Chapman (1998) and fall in the range of values deduced in the literature from simulations of the restratification of a convective basin (Table 1). The level of baroclinic instability is expected to decrease with horizontal model resolution. Decreasing the resolution to 5 km slows down the restratification in both OPA and MICOM-ADIAB ( $c_e = 0.028$ ) though without greatly altering the final buoyancy of the convective patch (not shown). Additionally, as the resolution becomes coarser, the difference between the restratification time scales in the two models becomes larger suggesting that the representation of baroclinic instability is more sensitive to the model physics when the internal radius of deformation is not adequately resolved.

### 3.3. Evolution of the water mass distribution

The evolution of the water mass distribution has been investigated based on the volume of each isopycnic layer inside and outside the convective patch (Fig. 7). The temperature distribution in OPA and in the ML in MICOM has been interpolated using a heat conserving scheme so as to reconstruct an equivalent distribution based on the prescribed temperature of the adiabatic isopycnic layers. Since this redistribution is fairly artificial for a deep ML which mixes properties between several layers, the pseudo-volumes of the corresponding isopycnic layers are plotted as dotted lines in Fig. 7 until the ML has actually reached the characteristics of the isopycnic layer. Given this redistribution, the volume of the convected water in all models appears to be initially contained in the 7th layer. The boundary between the “inner” volume and the “outer” volume is set at 70 km from the domain centre which corresponds to the limit of the initial convective cylinder. “Outer” volume variations should be exactly opposite to “inner” volume variations in a mass-conserving process. Note that the two volumes are normalized by the horizontal area of the inner domain so that “inner” volumes represent the actual layer thicknesses. The volume is divided into upper (layers 1–2), intermediate (layers 3–6), deep (layer 7), and bottom (layers 8–12) water masses.

At the end of the simulation, all models show a decrease of the deep water volume within the convective region. This decrease is the largest in MICOM where it is exclusively balanced by a corresponding increase of the volume of intermediate water. The process is fairly slow since it corresponds to a change in the ML characteristics which do not reach those of the intermediate waters before day 120 (Fig. 7b). In OPA and MICOM-ADIAB, the volumes of both upper and intermediate water masses increase as a result of the restratification. At the end of the restratification period, the “inner” volumes of the upper water masses are about the same in the two models but the volume of the intermediate (resp. deep) water masses is larger (resp. smaller) in OPA. The characteristic time scales of the volume evolution within the convective region are roughly the same for all water masses in both models. This suggests that restratification and dense water spreading have approximately the same characteristic time scale. This time scale is however shorter in OPA than in MICOM-ADIAB. Only the upper layers in OPA show a different behavior with a delay of some 20 days before the nominal characteristics of the layers are retrieved.

Considering the whole model domain, a substantial amount of intermediate waters is created in OPA. The mass gain for this water mass range within the convective patch is not compensated by an equivalent loss from the corresponding range outside the patch. Diapycnal processes must therefore be involved, most probably via exchanges across the front separating the convective patch from the outer region. From Fig. 7, one can postulate that the

**Table 1**

Various estimations of the eddy transfer efficiency across a density front surrounding a convective basin, as measured by the coefficient  $c_e$  (see explanation in text)

	Efficiency coefficient ( $c_e$ )	Dynamical concept	Reference
Theory	0.045	Ratio of the speed at which eddies propagate away from the front to the along front velocity (eddy dynamics assuming uniform potential vorticity)	Spall and Chapman (1998)
Unforced numerical experiments	0.03–0.046	Same as above	Spall and Chapman (1998)
	0.027	Restratification time scale in the convective patch	Jones and Marshall (1997)
Forced numerical or/and laboratory experiments	0.02	Restratification time scale in the vicinity of the rim current. (narrow front approximation)	Katsman et al. (2004)
	0.019–0.028	Equilibrium density anomaly of the convective patch for a given surface buoyancy loss	Spall and Chapman (1998)
	0.014–0.056	Equilibrium depth of the convective patch for a given surface buoyancy loss	Visbeck et al. (1996)

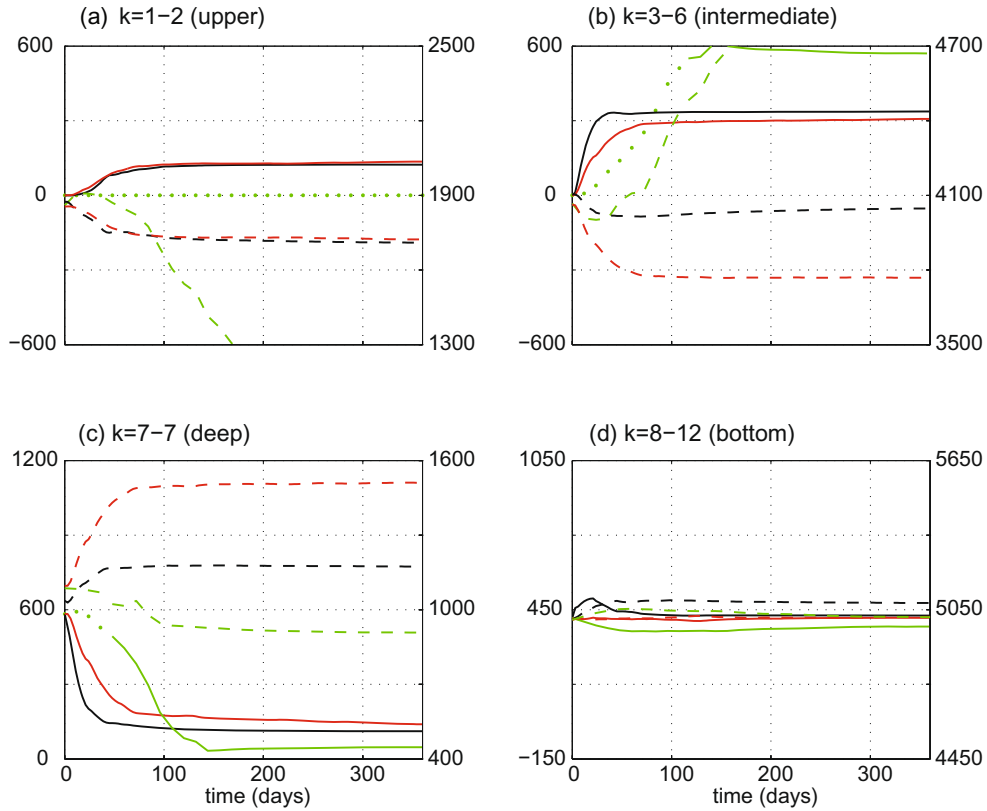


**Fig. 7.** Time evolution of the volume of each isopycnal layer in the central (cylinder of radius 70 km) (solid line, left axis) and outer (dashed line, right axis) regions for the four simulations shown in Fig. 6. Volumes are normalized by the area of the convective patch so as to represent thicknesses (in m). Dotted lines are used for MICOM as long as the properties of the “layer” do not match that of the corresponding isopycnal layer (see explanation in text). Colours as in Fig. 6. (For interpretation of colour mentioned in this figure the reader is referred to the web version of the article.)

340 m of intermediate waters created within the convective region are the result of lateral exchanges between the deep water (for 250 m) originally filling the convective patch, and the upper (for 20 m) and intermediate (for 70 m) waters from the outer region. An additional loss of 80 m of deep water volume is due to diapycnal mixing with the bottom layers (Fig. 7d). By contrast “inner” volume changes in MICOM-ADIAB are exactly compensated by “outer” volume changes in each water mass category as diapycnal mixing is negligible and stratification mainly changes through advection along isopycnals.

### 3.4. Distribution of the kinetic energy and instabilities

The different restratification time scales in the different models most probably relate to the different baroclinic instability. In order to investigate the role of eddies in the restratification process, the distribution of the eddy kinetic energy ( $K_E$ ) has been compared in the three simulations. In the definition of the mean and eddy components of the flow, a mass weighted average has been introduced which retains the information in terms of ocean layer thickness. For any variable  $\psi(r, \theta, k, t)$ ,  $r$  being the radial distance to the centre of the basin,  $\theta$  the azimuthal coordinate and  $k$  the layer index, this average can be written as  $\bar{\psi} = \overline{h\psi}/\bar{h}$ , where  $h(r, \theta, k, t)$  is the thickness of the  $k$ -layer and the overbar denotes spatial averaging. The associated fluctuations  $\psi'$  then verifies  $\overline{h\psi'} = 0$ . Note that  $h$  can be either the variable thickness of the layer in an isopycnal model or the constant level thickness,  $h_0$ , in a  $z$ -coordinate model, which in the latter case implies  $\bar{\psi} = \bar{\psi}$ .

On day 30, the radial symmetry of the initial stratification drives an upper cyclonic circulation and a deeper, weaker anticyclonic circulation around the convective patch (Fig. 8). The mean

circulation can thus be defined as an azimuthally averaged flow with a mean velocity,  $\bar{u}$ , defined as:

$$\bar{u}(r, k, t) = \frac{\int_0^{2\pi} h \bar{u} d\theta}{\int_0^{2\pi} h d\theta} \quad (3)$$

where  $\bar{u} = (u_r, u_\theta)$  is the horizontal velocity,  $u_r$  and  $u_\theta$  being its radial and azimuthal components. According to the flow geometry, one expects a mainly azimuthal flow verifying  $\bar{u}_\theta \gg \bar{u}_r$ .

The mean kinetic energy of a layer  $k$  of mean thickness  $\bar{h}$  is:

$$K_M(r, k, t) = \frac{1}{2} \rho_0 \bar{h} (\bar{u}_r^2 + \bar{u}_\theta^2) \quad (4)$$

where  $\rho_0$  is a reference density taken to  $10^3 \text{ kg m}^{-3}$ , while the eddy kinetic energy is:

$$K_E(r, k, t) = \frac{1}{2} \rho_0 \overline{h(u_r'^2 + u_\theta'^2)} - K_M(r, k, t) = \frac{1}{2} \rho_0 \overline{h(u_r'^2 + u_\theta'^2)} \quad (5)$$

Contrasted distributions of the eddy kinetic energy are found between models (Fig. 9). In MICOM, the kinetic energy is concentrated at the base of the ML where the isopycnal surfaces are the steepest. Very little energy is found elsewhere, most notably in the ML where vertical shears, and therefore baroclinic instability, cannot be resolved due to the assumed vertical homogeneity of the flow properties. By contrast, in both MICOM-ADIAB and OPA,  $K_M$  is surface intensified. The radial structure of  $K_M$  in OPA shows several vertical bands in which the energy decreases from the surface to the bottom. In MICOM-ADIAB, rather than a continuous feature in the vertical, a vertical dipole is found with a distinct extremum of energy at depth ( $\sim 500 \text{ m}$ ), at the level where the

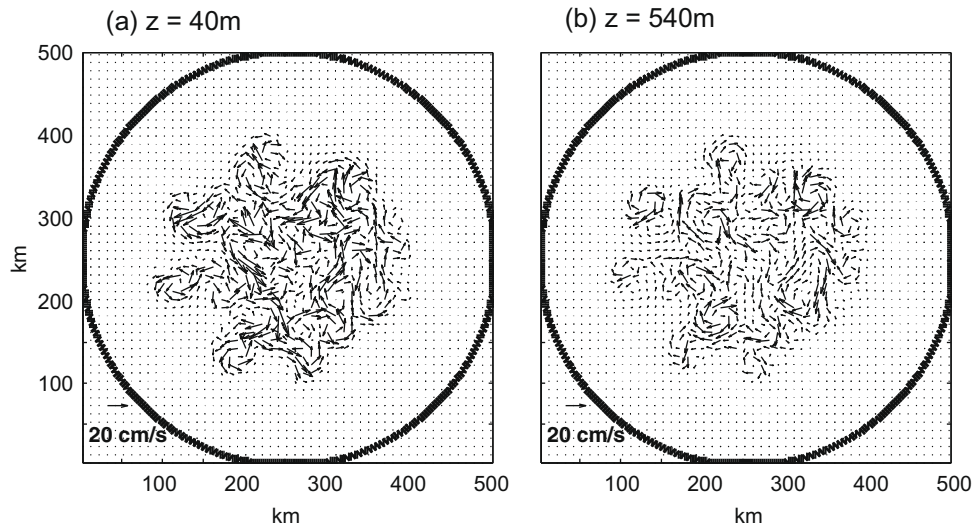


**Fig. 8.** Horizontal velocity (in  $\text{cm s}^{-1}$ ) averaged over (a) the uppermost 83 m, and (b) the layer 500–583 m, on day 30 in MICOM-ADIAB.

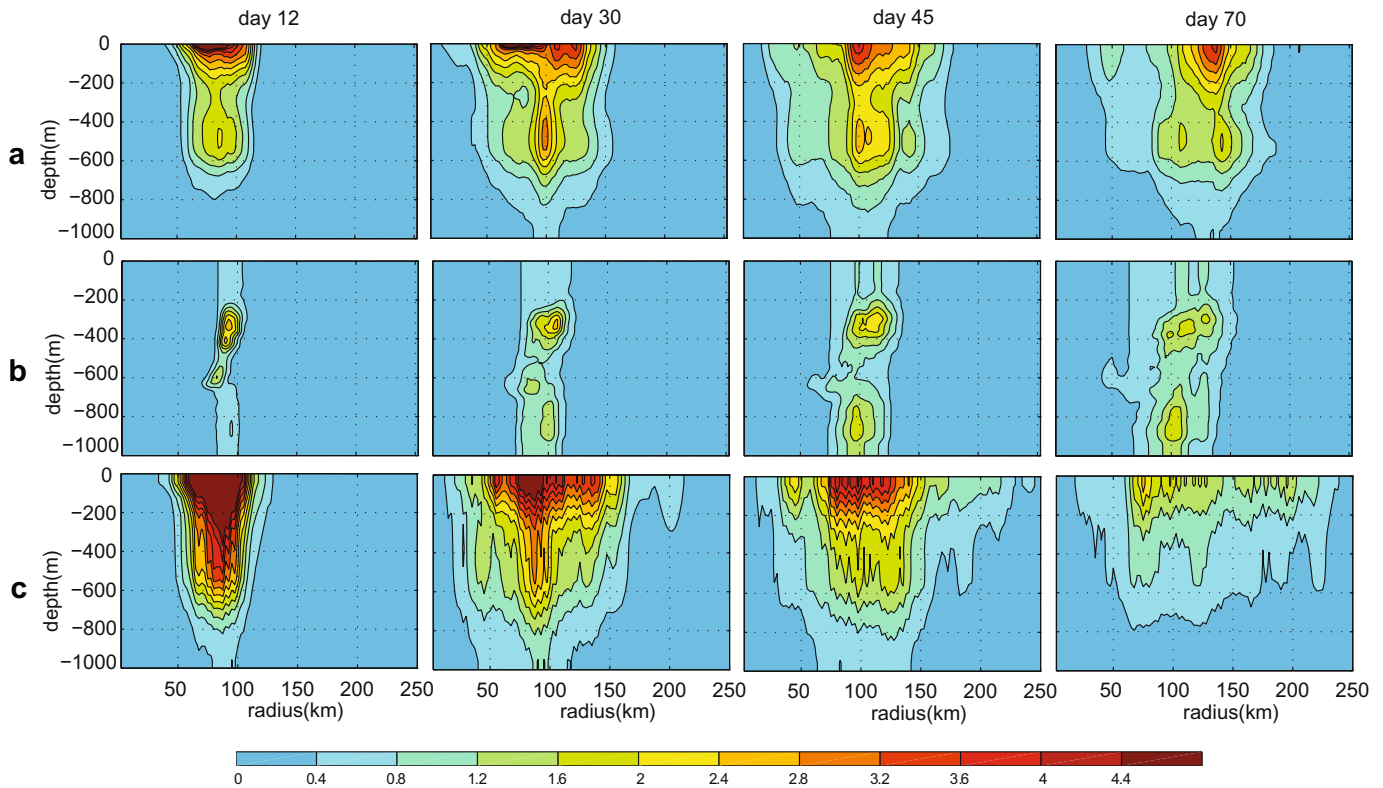


**Fig. 9.** Vertical distribution of the eddy kinetic energy (in  $10^6 \text{ J m}^{-2}$ ) as a function of the distance to the centre of the basin for (a) MICOM-ADIAB (b) MICOM, and (c) OPA. Energy values are obtained through azimuthal integration. Note that energies plotted in (b) have been multiplied by 3.

dense water is expected to spread away from the convective region. The kinetic energy in the water column indeed appears to be concentrated along the tilted boundary separating the dense homogeneous water from the upper and intermediate stratified layers.

In MICOM, the evolution of the energy maximum shows an outward spreading following the evolution of the layer thickness gradients (Fig. 9). In the other two models, the energy spreads both outward and inward with time, at all depths. Still, in OPA, the eddy field extends farther outward than in MICOM-ADIAB.

Both the energy level and the growth rate are much larger in OPA and MICOM-ADIAB than in MICOM (Fig. 10). Averaged over the basin area, the energy does not reach a maximum before day 90 in MICOM while this maximum is reached earlier in the other two models. In both OPA and MICOM-ADIAB, the maximum occurs on day 30 at the surface but while the kinetic energy in OPA shows the same time evolution throughout the whole water column, in MICOM-ADIAB the energy grows more slowly and more persistently at depth, reaching a maximum not before day 45.

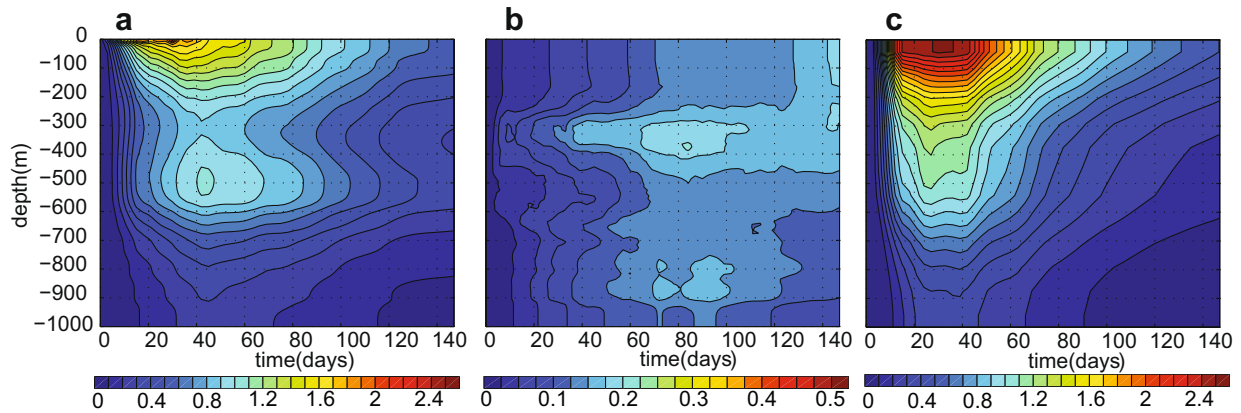


**Fig. 10.** Time-depth distribution of the eddy kinetic energy (in  $\text{J m}^{-2}$ ) averaged over the whole basin area for (a) MICOM-ADIAB, (b) MICOM, and (c) OPA.

Baroclinic instability builds on conversion of potential energy into eddy kinetic energy. Part of the potential energy of the mean large scale flow,  $P_M$ , is transferred to the eddy scales through a rearrangement of the mass field, thus creating eddy potential energy ( $P_E$ ) which, in turn, is converted into kinetic energy. In  $P_M$ , we consider only that part of the mean potential energy (the so-called available potential energy or APE) which can be recovered for energy conversions. In isopycnal coordinates, an estimate of the mean and eddy APE can be calculated from the displacements of the isopycnal surfaces relative to a horizontally uniform reference state. The latter is obtained after a complete adiabatic leveling of the isopycnal surfaces in which mass is conserved (e.g., Housais, 1984). For a layer interface  $k$  at a mean depth  $\bar{z}_k$  these can be written as:

$$P_M(r, k, t) = \frac{1}{2} g \Delta \rho_k (\bar{z}_k - z_{\text{ref}})^2 \quad (6)$$

$$P_E(r, k, t) = \frac{1}{2} g \Delta \rho_k \bar{z}_k^2 \quad (7)$$

where  $\Delta \rho_k$  is the density jump across the interface,  $z'_k$  is the deviation of the interface depth from its mean and  $z_{\text{ref}}$  is the depth of the interface in the reference state. Alternatively, in a  $z$ -coordinate frame, direct estimate of the isopycnal displacements is no longer possible and the mean and eddy APE of a layer of fixed thickness  $h_0$  are estimated as (e.g., Oort et al., 1989):

$$P_M(r, k, t) = \frac{1}{2} g h_0 \frac{1}{\partial \rho / \partial z|_{\text{ref}}} (\bar{\rho} - \rho_{\text{ref}})^2 \quad (8)$$

$$P_E(r, k, t) = \frac{1}{2} g h_0 \frac{1}{\partial \rho / \partial z|_{\text{ref}}} \bar{\rho}^2 \quad (9)$$

where  $\frac{\partial \rho}{\partial z}|_{\text{ref}}$  is the vertical density gradient in the reference state while  $\bar{\rho}$  and  $\rho'$  are the mean density and the deviation from this mean at the  $k$ -level, respectively. In order to have consistent diagnostics,  $\rho_{\text{ref}}$  in OPA is deduced from a linear interpolation, onto the  $k$ -levels, of the isopycnal values defining the reference state in MICOM-ADIAB.

We focus our attention on the first 100 days of the simulations before dissipation processes lead to a general decrease of all types of energy (Fig. 11). In all three models, the first days of the simulation bring out a fast geostrophic adjustment during which the large amount of potential energy (ca.  $8000 \text{ J m}^{-2}$ ) initially stored in the steep isopycnals surrounding the convective patch is rapidly made available for the build-up of a rim current (Fig. 8). At that time,  $K_M$  is about the same in OPA and MICOM-ADIAB ( $80\text{--}100 \text{ J m}^{-2}$ ) but is twice as large as in MICOM ( $40 \text{ J m}^{-2}$ ). The following days are marked by a joint increase of the eddy potential energy and eddy kinetic energy. The growth of  $P_E$  is associated with an energy trans-

fer from  $P_M$  but some of this energy production is converted into eddy kinetic energy through baroclinic instability contributing to the concomitant growth of  $K_M$ . Judging from the evolution of  $K_M$ , the barotropic conversions should be much less efficient than the baroclinic conversions in all three models with the former being more continuous in MICOM, than in OPA and MICOM-ADIAB.

The slower growth and smaller level of eddy kinetic energy in MICOM occurs despite the high level of eddy potential energy. In fact, instead of the expected decrease, the total potential energy remains at a high level or even increases gradually after 80 days, obviously in relation to the ML dynamics. However, little of this energy reservoir is actually made available for baroclinic conversion into eddy kinetic energy. A careful examination of the different contributions to the potential energy increase reveals that half of it is due to the mass rearrangement associated with the ML deepening at the rim of the convective patch while the other half is due to exchange between the dense ML water from the interior of the convective patch and the light water at the periphery. Since the ML base is not an isopycnal surface, vertical displacements associated with rearrangements of the ML mass involve water with contrasted properties and may therefore be responsible for spurious potential energy variations. The process of water mass exchange between the convective patch interior and the surroundings in MICOM is indeed opposite to the one occurring in the other two models: outward spreading of relatively dense water takes place in the upper layer while the gain of buoyancy in the interior region occurs at depth underneath the ML. Since the impact of the former process on the potential energy dominates over the latter, the resulting effect is an increase of the overall potential energy.

OPA and MICOM-ADIAB are close to each other in terms of eddy energy evolution. In particular, the two models maintain approximately the same level of eddy potential energy until day 40. A noticeable difference is however seen in the faster but less persistent growth of the eddy kinetic energy in OPA, which results in a higher kinetic energy level until day 60 and lower afterwards. More specifically,  $K_E$  grows faster during the first 15 days, reaching a maximum value of  $1140 \text{ J m}^{-2}$  around day 30, while in MICOM-ADIAB, a more persistent but slower growth leads to a maximum of  $850 \text{ J m}^{-2}$  for  $K_E$  delayed until day 45. Part of the reduced energy growth in MICOM-ADIAB during the early stage of the simulation may be due to larger dissipation rates (Fig. 12) as the Smagorinsky parameterization of viscosity in this model tends to increase friction in regions of large flow deformation rates, i.e., mainly in the unstable frontal region. From day 45 onwards, however, dissipation is very similar between the two models (Fig. 12) and the observed differences between the kinetic energy evolutions must relate to different production rates, essentially through more per-

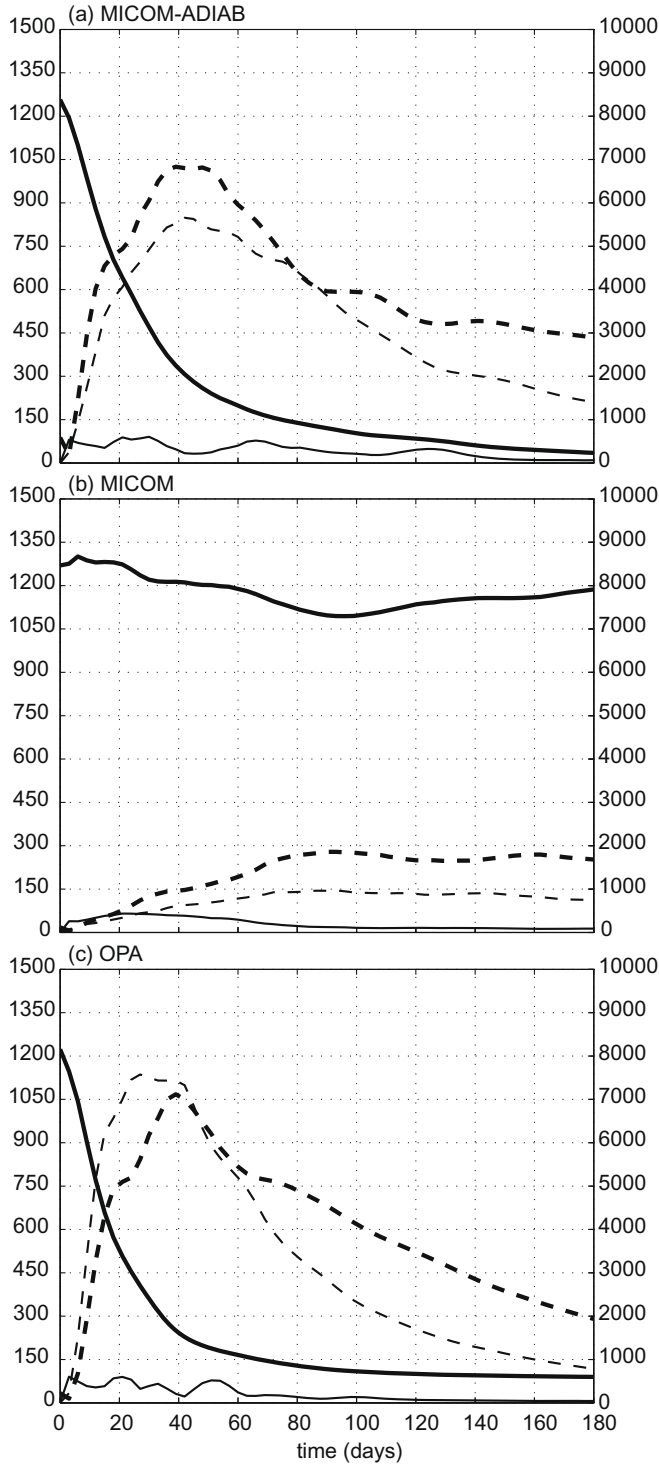


**Fig. 11.** Time evolution of the vertically (top to bottom) integrated mean (solid line) and eddy (dashed line), kinetic (thin line), and available potential (bold line) energies averaged over the whole basin area (in  $\text{J m}^{-2}$ ) for (a) MICOM-ADIAB (b) MICOM, and (c) OPA. The right axis corresponds to the mean available potential energy in the three models and also to the eddy available potential energy in MICOM. The left axis corresponds to the other energies. Note that in MICOM, the density and velocity fields are interpolated on fixed vertical coordinate (every 10 m) before being used to calculate the energies.

sistent baroclinic instability in MICOM-ADIAB. When compared to OPA, a higher level of potential energy is indeed more or less continuously maintained in MICOM-ADIAB during the first 70 days of the simulation which suggests a different timing of the energy conversions.

Energy conversions provide a quantification of the strength of the instabilities and help characterizing their nature. The eddy potential energy calculated in isopycnic coordinates (Eqs. (6), (7)) is not directly comparable to that calculated in isobaric coordinates (Eqs. (8), (9)) (Bleck, 1985) unless, as proposed by Bleck (1985) the potential energy  $P$  is split into its mean and eddy components. Since none of the coordinate systems allows direct exchange between  $P_M$  and  $K_M$ , conversions from  $P$  to  $K_E$  can still be interpreted as conversions between  $P_E$  and  $K_E$ . Additionally, such a simplification allows one to ignore the details of the energy transfers from  $P$  to  $K_E$  which in isopycnic coordinates follow a slightly different pattern (involving the mean kinetic energy) from the one in isobaric coordinates as defined by Lorentz (1967) (see Bleck, 1985 for a more complete explanation).

Accordingly, the conversion rate from  $P$  to  $K_E$  can be written as:

$$C(P, K_E) = \rho_0 (\overline{h\bar{u}' \cdot \nabla_k (\phi + p^* \alpha)} - \overline{\nabla_k \cdot (h\bar{u}' \phi)}) \quad (10)$$

while the conversion from  $P$  to  $K_M$  is:

$$C(P, K_M) = \rho_0 (\overline{h\bar{u}' \cdot \nabla_k (\phi + p^* \alpha)} - \overline{\nabla_k \cdot (h\bar{u}' \phi)}) \quad (11)$$

and the conversion from  $K_M$  to  $K_E$  is:

$$C(K_M, K_E) = -\rho_0 \overline{h\bar{u}' \cdot (\bar{u}' \cdot \nabla_k) \bar{u}} \quad (12)$$

in which  $\alpha(k)$  is the specific volume of a  $k$ -layer,  $\phi(k) = -g\rho_0 \sum_{k'=1}^{k-1} \alpha(k')h(k')$  the geopotential,  $p^*(k) = g\rho_0 \sum_{k'=1}^{k-1} h(k')$  the depth of the upper interface of this layer in pressure units, and  $\nabla_k$  is the horizontal gradient operator following this layer. To take into account the free surface, a correction is added to both  $\phi$  and  $p^*$  so that:

$$\phi(k) = g\rho_0 \left[ -\sum_{k'=1}^{k-1} \alpha(k')h(k') + \alpha(k)z_{\text{surf}} \right] (1 + \eta) \quad (13)$$

where  $z_{\text{surf}}$  is the sea surface elevation (positive downward) and  $\eta$  represents the barotropic correction to a baroclinic ocean:

$$\eta = \frac{\rho_0}{p_b^*} (gz_{\text{surf}} - M(1)) \quad (14)$$

with  $M(k)$  being the Montgomery potential in the  $k$ -layer, and  $p_b^* = \rho_0 g H_b$  the baroclinic pressure at the bottom.

In  $z$ -coordinates, the conversions terms can be expressed as:

$$C(P, K_E) = -gh\bar{w}'\bar{\rho}' - gh\nabla \cdot (\bar{v}'\bar{p}') \quad (15)$$

$$C(P, K_M) = -gh\bar{w}\bar{\rho} - gh\nabla \cdot (\bar{v}\bar{p}) \quad (16)$$

$$C(K_M, K_E) = -\rho_0 \overline{h\bar{u}' \cdot (\bar{u}' \cdot \nabla_z) \bar{u}} \quad (17)$$

where  $\bar{v}$  is the three-dimensional velocity,  $w$  its vertical component,  $p$  is the pressure, and  $\nabla$  and  $\nabla_z$  are the three-dimensional and horizontal (following the isodepths) gradient operator, respectively.

In Fig. 12, baroclinic conversions are only shown for MICOM-ADIAB and OPA. The time evolution of the APE in MICOM (Fig. 11b), especially its persistent high level throughout the simulation, suggests that the mechanisms controlling the potential energy variations are not adequately represented in this model (see preceding discussion on Fig. 11). In particular, these variations not only reflect the baroclinic conversions but also hydrostatic instabilities which occur more or less continuously at the base of the dense ML at the rim of the convective patch, acting as a permanent potential energy sink.

The radial distribution of  $C(K_M, K_E)$  (not shown) shows that the barotropic instability occurs at the limit of the frontal region in all three models. In MICOM, it is the more active right at the mixed layer base where the isopycnic layer interfaces are the steepest and, therefore, the horizontal velocity shears are the largest. In both OPA and MICOM-ADIAB,  $C(K_M, K_E)$  is rather char-

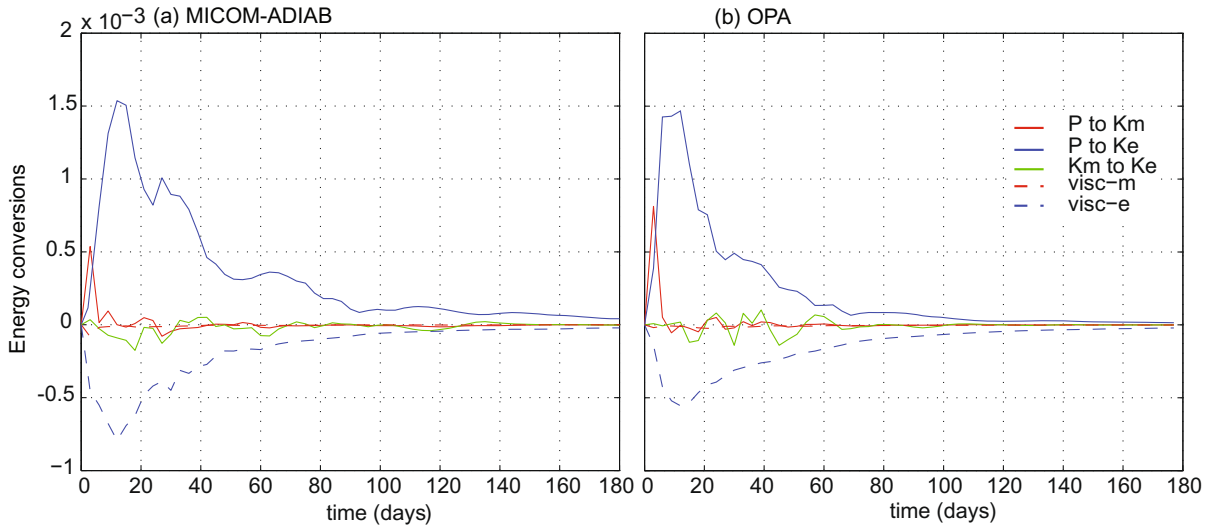


**Fig. 12.** Time evolution of the vertically (top to bottom) integrated energy conversion rates averaged over the whole basin area (in  $W m^{-2}$ ) for (a) MICOM-ADIAB, and (b) OPA.  $C(P, K_M)$  in red,  $C(P, K_E)$  in blue,  $C(K_M, K_E)$  in green. Dashed red (resp. blue) line corresponds to the change in mean (resp. eddy) kinetic energy due to viscosity. (For interpretation of colour mentioned in this figure the reader is referred to the web version of the article.)

acterized by a surface intensified signal which oscillates in time. As already suggested by the evolution of the mean kinetic energy, the transfer from  $K_M$  to  $K_E$  in these two models is small compared to the baroclinic conversions  $C(P, K_E)$ . In both models, the latter shows a peak of about  $1.5 \cdot 10^{-3} W m^{-2}$  on day 13, followed by a period of rapid decrease until day 20. The two models however differ with regards to the timing of the maximum and the subsequent evolution of the energy production. The baroclinic production of energy in OPA is persistently larger in the early stage of the instability growth to its maximum, a larger eddy kinetic energy production of  $1250 J m^{-2}$  is actually found in OPA compared with MICOM-ADIAB ( $900 J m^{-2}$ ). Following the maximum of the baroclinic conversion, however, a more rapid decrease occurs in OPA while energy conversion shows larger persistency in MICOM-ADIAB. A comparison of the time evolutions of the conversion rates (Fig. 12) and of the energies (Fig. 11) gives more insight into the processes at work during

that period. Compared to MICOM-ADIAB, the smaller baroclinic conversions in OPA are indeed associated with a faster decrease of the eddy potential energy between day 40 and day 80, and a concomitant slower decrease of the mean potential energy, which altogether suggest that baroclinic conversions are inhibited by a slower potential energy cascade toward the eddy scale. Taking into account the effect of dissipation would not alter this conclusion as potential energy dissipation appears to be equivalent in the two models from day 40 onwards. By contrast, the persistent decrease of the mean potential energy in MICOM-ADIAB during the same period suggests that the energy cascade is still active and able to maintain a high level of kinetic energy production through baroclinic instability.

3.5. Lateral heat fluxes

The mean basin circulation being primarily azimuthal, eddies must be responsible for carrying heat into the convective patch

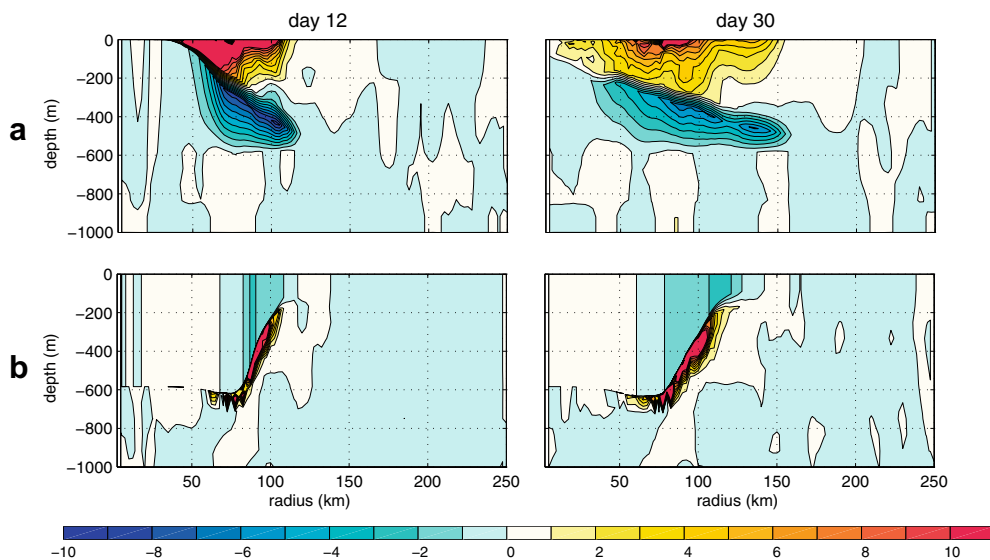


**Fig. 13.** Vertical distribution of the azimuthally integrated horizontal eddy mass flux (in  $10^3 m^2 s^{-1}$ ) as a function of the distance to the centre of the basin for (a) MICOM-ADIAB and (b) MICOM.

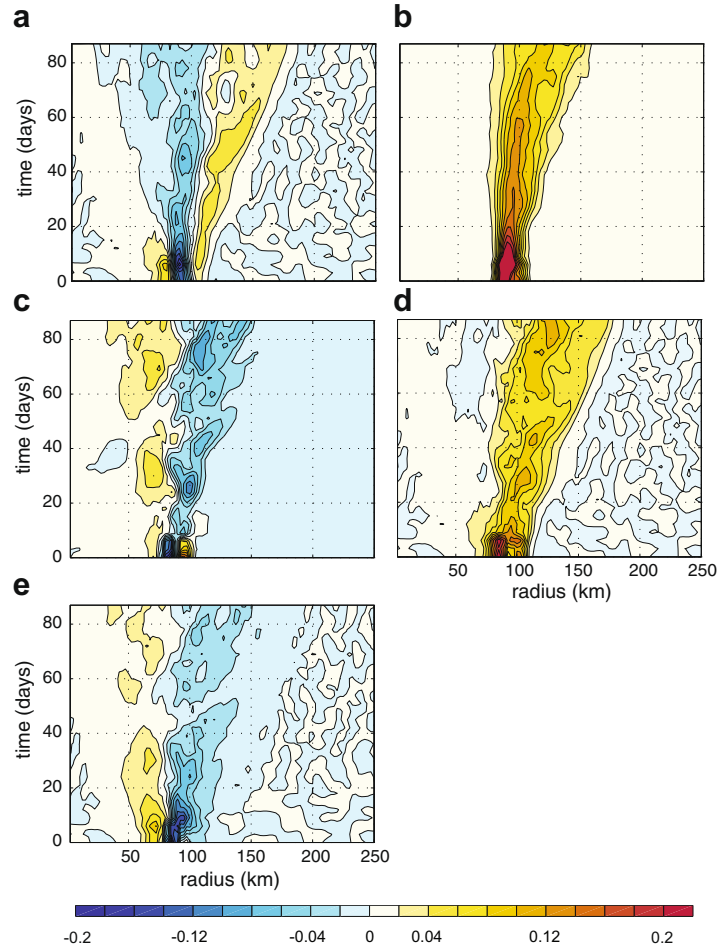


**Fig. 14.** Time-radial distance distribution of the azimuthally integrated contributions to the change in ML heat content (in  $10^9 \text{ W m}^{-1}$ ) in MICOM: (a) mass flux convergence, (b) hydrostatic instability, (c) temperature advection, (d) sum of the three contributions. Also shown in (e) is the heat flux convergence integrated over the whole water column. In (a), (b), and (d) the scale should be multiplied by 10.

and exporting cold water outside. The comparable time evolutions of  $C(P, K_E)$  and of the buoyancy (Fig. 6), both suggesting more rapid restratification in OPA, demonstrate the crucial role of the baroclinic instability. For a layer of thickness  $h$ , the lateral eddy heat flux across the lateral boundary of a cylinder of radius  $r$  and unit height can be written as:

$$F(r, k, t) = \int_0^{2\pi} -u'_r T' r d\theta \quad (18)$$

where  $u'_r$  is the eddy radial velocity component taken positive outward, and  $T'$  is the temperature fluctuation. In the two isopycnic models, as for the eddy kinetic energy, the vertical distributions of  $u'_r$  and  $T'$  are obtained through projection of the isopycnic velocity and temperature distributions onto a fixed  $z$ -coordinate framework.

In the two isopycnic models, the lateral eddy heat flux  $F$  is associated with a differential mass transport. In MICOM-ADIAB (Fig. 13a), the differential is established between a surface (resp. deep) mass convergence and a deep (resp. surface) mass divergence inside (resp. outside) the convective patch. This differential represents the distinct processes of surface capping, by formation of a new upper layer, and deep water spreading. In MICOM (Fig. 13b), the mass differential is inverted compared with MICOM-ADIAB, as the ML spreads outward and an inward mass flux fills the intermediate layers underneath the ML. This mass exchange is the only way for the model to handle the retreat of an

originally deep mixed layer. Still, if the vertical integral is considered, the net effect of these lateral mass fluxes (Fig. 14a) is not the main contributor to the heat exchange (Fig. 14d). Diapycnal mass transfers associated with hydrostatic instability at the ML base (Fig. 14b), tend to redistribute vertically the advected anomalies. This redistribution dominates the deepening of the ML at the outer rim of the homogeneous patch. Concomitantly, it opposes the retreat of the ML inside the patch (compare Fig. 14a with b) erasing the signature of unstable thermocline eddies and thus preventing inward penetration of the associated heat fluxes. Lateral advection of temperature anomalies within the ML (Fig. 14c) also contributes to the ML heat content evolution. This latter contribution is smaller than the other two but, when considering the entire water column, it appears to dominate the overall warming (resp. cooling) of the convective (resp. outer) region (compare Fig. 14c and e).

In all three models, the maximum of the lateral heat transfer follows the outer limit of the convective patch (Fig. 15). In MICOM, eddy heat fluxes are mainly concentrated within the ML, but they are very small (Fig. 15b), consistent with the very slow changes in the ML properties observed in Fig. 4b. MICOM-ADIAB exhibits the strongest heat flux maxima among the three models as a result of more persistent lateral density gradients in the isopycnic framework. Two poles are clearly distinguishable (Fig. 15a). The stronger, aligned with the lower interface of the upper stratified layers, represents the inward heat transport associated with the surface/intermediate restratification of the convective patch. The feature progressively extends further inward. A weaker, deeper pole in

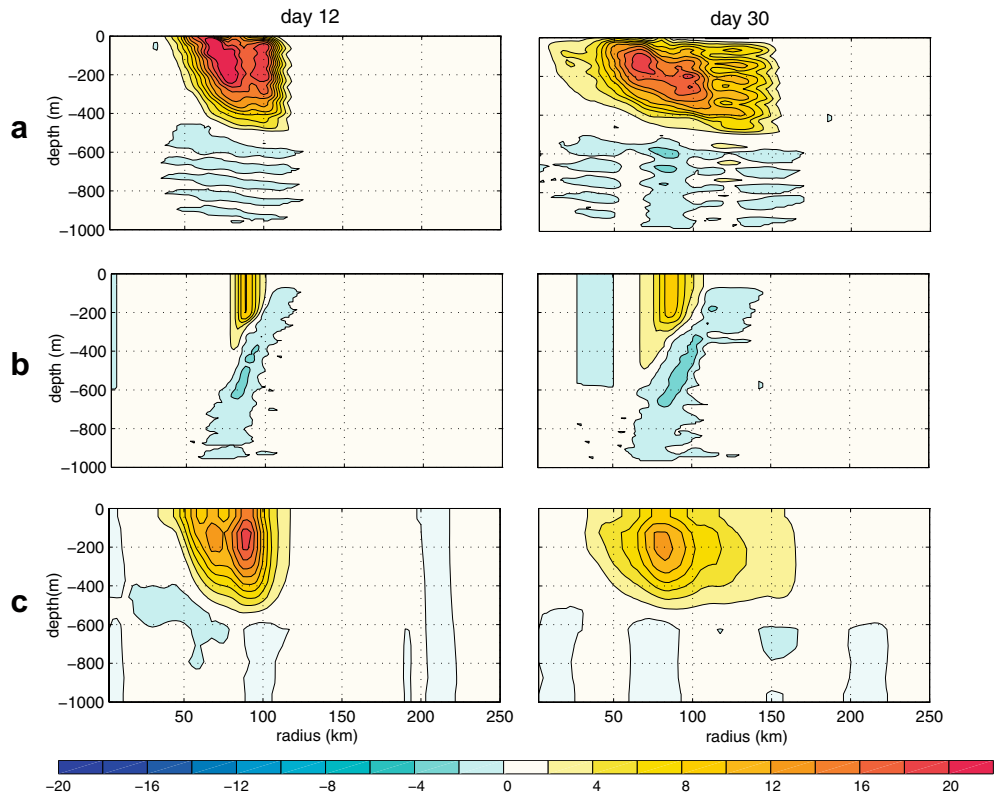


Fig. 15. Vertical distribution of the azimuthally integrated horizontal eddy heat fluxes (in  $10^6 \text{ W m}^{-2}$ ) for (a) MICOM-ADIAB, (b) MICOM, and (c) OPA.

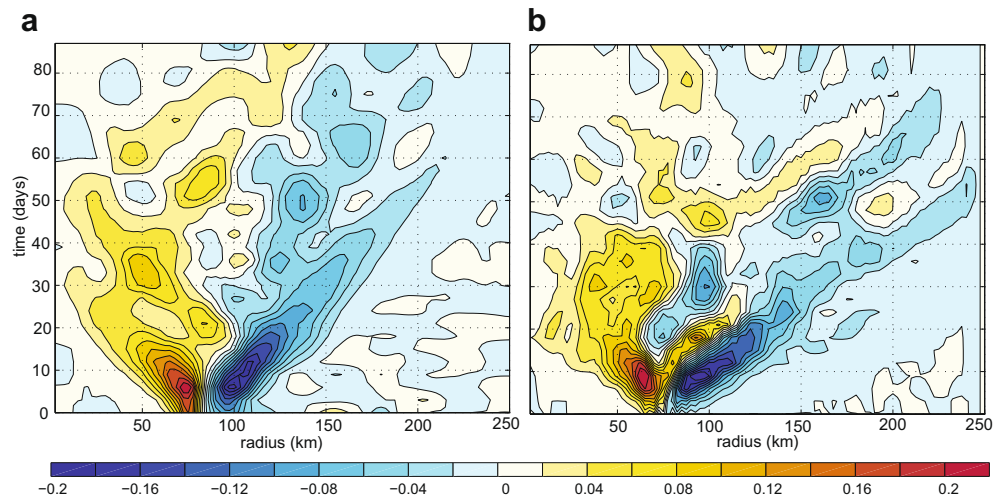
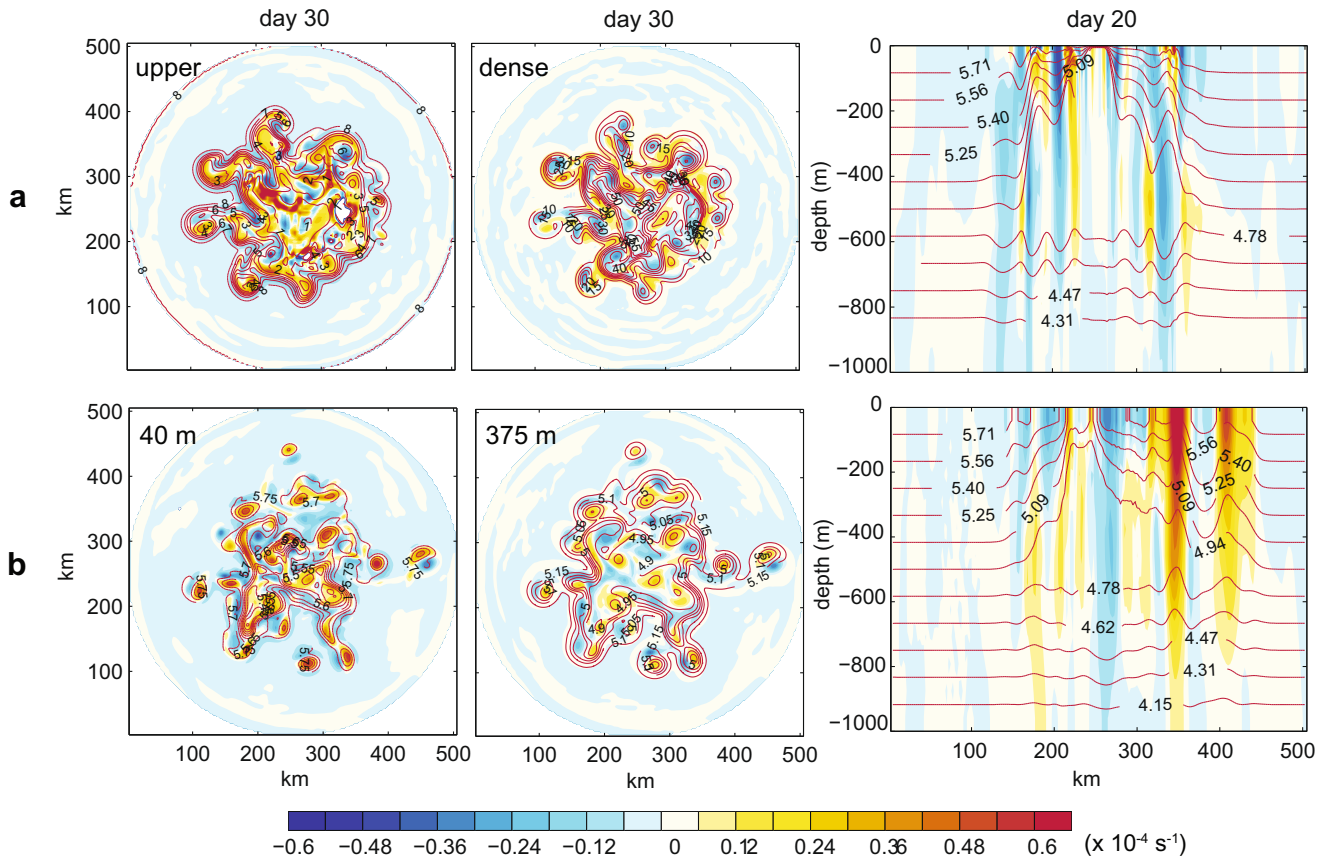


Fig. 16. Time-radial distance distribution of the azimuthally and vertically integrated convergence of the eddy heat fluxes (in  $10^9 \text{ W m}^{-1}$ ) for (a) MICOM-ADIAB, and (b) OPA.

the outer region initially spreads across the 50–250 m layer but progressively deepens and moves outward. This deeper signal is linked to upward displacements of the dense water interface in the outer region associated with dense water spreading. In OPA, the initial two poles structure merges into a single signal enhanced at intermediate depth ( $\sim 200 \text{ m}$ ) (Fig. 15c). The absence of a distinct deep signal is consistent with the predominant reformation of intermediate layers diagnosed in Figs. 4c and 7b and attributed to the effect of diapycnal exchanges across the density front surrounding the convective patch.

The magnitude of the heat flux convergence is very comparable in OPA and MICOM-ADIAB (Fig. 16). In OPA, vertical heat transfers (not

shown here) due to surface convergences (resp. divergences) occurring in cold (resp. warm) core eddies add some contribution to the surface warming. Additionally, downward (resp. upward) heat transport associated with downward (resp. upward) gradients of temperature anomalies induce an overall cooling from the surface down to 500 m. These vertical contributions are however smaller than the contribution from the horizontal exchanges and the resulting heat flux convergence leads to fairly uniform warming of the upper 500 m within the patch and cooling of this layer outside. In MICOM-ADIAB, the warming-cooling pattern is more contrasted in the vertical with the inner warming confined to the upper layers and the outer cooling concentrated in the intermediate and deep layers.



**Fig. 17.** Horizontal distribution of relative vorticity (in  $10^{-4} \text{ s}^{-1}$ , coloured scale) on day 30 (left two panels) and distribution of relative vorticity and temperature ( $^{\circ}\text{C}$ ) on a section through the centre of the basin on day 20 (right two panels) for (a) MICOM-ADIAB and (b) OPA. In the left panels, vorticity is plotted (a) for the uppermost (layer 1) and dense (layer 7) layers superimposed with isolines of the corresponding layer thickness and (b) at selected depth levels (40 m and 375 m) superimposed with isolines of the temperature ( $^{\circ}\text{C}$ ).

In MICOM, the inward and outward spreading of the signal is very slow so that little heat is actually transported away from the boundary of the convective patch (Fig. 14e). In the other two models (Fig. 16), the heating signal propagates inward at about the same rate during the first 10 days but, after day 10, the spreading accelerates in OPA so that eddy heat fluxes already reach the centre of the basin on day 20, some 15 days earlier than in MICOM-ADIAB. OPA also shows a more rapid cooling signal outside the convective patch than MICOM-ADIAB. The signal propagates over 70 km in 25 days while the same distance is performed in almost 35 days in MICOM-ADIAB.

The lateral spreading of the eddy kinetic energy is similar to that of the eddy heat flux while in the vertical, the matching is not as good, at least in OPA (compare Fig. 9 and Fig. 15). For instance, on day 30, larger eddy heat fluxes occur at intermediate depths ( $\sim 200$  m) (Fig. 15), most probably related to the strongest temperature fluctuations at that level, despite the eddy kinetic energy remains surface intensified (Fig. 9). In MICOM-ADIAB, the distribution of the layer thickness fluctuations is expected to best correlate with the distribution of eddy kinetic energy, essentially because the vortex stretching of the mean flow controls the regions of energy production. Isopycnic and  $z$ -coordinate models in fact generate eddy fields with somewhat different characteristics. In MICOM-ADIAB, the warm core anti-cyclonic eddies in the upper layers transport heat inward while the outside cooling is performed by cold core cyclonic (in the upper layers) and anti-cyclonic (in the deep layer) eddies (Fig. 17a, right panel). In OPA, the eddy field tends to be more

barotropic (Fig. 17b, right panel), a feature which can be explained by secondary eddy induced circulations (Madec et al., 1991). The lateral heat transport is therefore expected to be more uniform in the vertical although temperature gradients enhance the signal at mid-depth. At all levels in this model, cold core cyclonic eddies are more efficient than warm core anti-cyclonic eddies in transporting heat from the outer region to the centre of the basin. The horizontal distributions of the relative vorticity (Fig. 17, left panels) also show numerous occurrences of eddies shedding from the rim current toward the basin periphery which are not seen in MICOM-ADIAB.

#### 4. Discussion

Bulk mixed layer models, such as the one included in the MICOM model, are known to perform reasonably well during the mixing phase of the convection, at least in the early stages when advection effects are not too important (e.g., Marshall and Schott, 1999). The present study shows that a bulk ML embedded in a three dimensional isopycnic model does not adequately simulate the restratification phase in the absence of surface forcing, essentially because the physics of the lateral exchanges in the upper water column are not satisfactorily represented. One of the main shortcomings of these models is related to the fact that reformation of the light upper layers can only be achieved once the ML has itself reached the properties of these light waters, a condition which makes the process oversensitive to the timing and amplitude of the atmospheric surface buoyancy flux. When the latter is ignored as in the present study, purely horizontal advection/dif-

fusion in the ML is unable to reconstruct the desired properties of the surface layers while persistent hydrostatic instabilities at the ML base hamper dynamical retreat of this layer. Since ML physics assume vertical homogeneity of the dynamical properties, as long as a deep ML persists, the vertical contrasts remain unresolved in a large portion of the upper water column. On the other hand, the domain where purely isopycnal physics are effective is restricted to the deeper, and therefore less dynamical layers underneath the ML. Consequently, baroclinic instability, yet known to play a crucial role in the first stages of the restratification, cannot be adequately represented. These conclusions are consistent with earlier model intercomparison studies focusing on frontal dynamics (Eldevik, 2002). Assumed vertical homogeneity in the ML also inhibits development of ML instabilities (Boccaletti et al., 2007) which feed on the slumping of ML density fronts often developing in response to spatial heterogeneities of the surface forcing. Additionally, these instabilities occur on spatial scales which are too short to be resolved by our models. A deformation radius equal to the smallest resolved length scale of 5 km, would correspond to a stratification  $N \approx 10^{-3} \text{s}^{-1}$  which is much stronger than the central domain stratification.

Among the three model physics explored, the adiabatic isopycnal physics show the most realistic final stratification, allowing the persistence of a lens of convected dense water in agreement with observations (Send et al., 1995; Lilly et al., 1999). The distinct processes of surface capping and deep spreading are well reproduced in contrast to the  $z$ -coordinate model which shows unrealistic formation of intermediate water masses to the detriment of the dense water reservoir. A shorter restratification time scale as observed in OPA therefore should not be interpreted as a sign of a more efficient restratification. The better performance in terms of stratification is indeed expected from a model in which isopycnal advection-diffusion guarantees preservation of water mass properties. By contrast, both horizontal diffusion and horizontal advection inherent to  $z$ -coordinate models are known to lead to spurious diapycnal mixing, especially in frontal regions. Rotating the diffusion tensor to allow diffusion to operate along isoneutral surfaces or using a higher order advection operator could in principle reduce these spurious effects. These two modifications have been tested independently in the OPA code, still they did not provide a real improvement of the solution in terms of density distribution. Neither replacement of the standard centred-difference advection scheme by a higher order (TVD, Total Variation Diminishing) advection scheme in the tracer equation nor the change to isopycnal diffusion did bring the stratification in OPA closer to that in MICOM-ADIAB. The differences in the eddy kinetic energy evolution also persist between the two models: in all OPA sensitivity experiments the eddy kinetic energy grows faster and with less persistency than in MICOM-ADIAB.

The faster growth of the eddy kinetic energy in the early stage of the instability in the  $z$ -coordinate model, which leads to a higher kinetic energy level during the first 60 days of the simulation, is consistent with similar conclusions drawn from diagnoses of the eddy activity in eddy-permitting models of the North Atlantic circulation (Willebrand et al., 2001; Barnier et al., 2001). However, it was unclear in these studies whether the discrepancy should be attributed to less energy production or more energy dissipation. Examination of the source and sink terms in the kinetic energy equation shows that a smaller energy conversion rate in the very early days of the instability and higher energy dissipation in regions of high flow deformation during the first 40 days of the instability may both contribute to the lower kinetic energy level in MICOM-ADIAB during that period. On the other hand, sensitivity experiments in which the Smagorinsky coefficient is doubled in MICOM-ADIAB or the viscosity is multiplied by 3 in OPA, produce

almost unchanged production rates, suggesting that viscosity only affects the energy dissipation without altering much the energy production. Similarly, only slight differences are observed in the  $K_E$  production in OPA when changing the representation of the advection diffusion as in the sensitivity experiments discussed in the preceding paragraph, or when dividing the explicit tracer diffusion by 3 using the TVD scheme. This may however be not as true for MICOM-ADIAB where the implicit diffusion in the FCT advection scheme used for the layer thickness equation may contribute to the reduced baroclinic conversions observed in the very early stage of the instability. This implicit diffusion should however be fairly small in our particular simulation where outcropping of isopycnals maintain a high degree of baroclinicity (Griffiths et al., 2000).

The different evolutions of the baroclinic energy production in OPA and MICOM-ADIAB therefore appear to be mainly a consequence of the different model physics. Generation of spurious vorticity in the  $z$ -coordinate models due to an advection scheme which does not conserve potential vorticity, appears as the most plausible mechanism for the overestimated growth in the early stage of the instability (Drijfhout, 1992). Increasing the vertical resolution should reduce the overestimation (e.g., Ikeda and Wood, 1993), as apparently, the vertical resolution chosen in our experiments is not fine enough to entirely remove such spurious effects. On the other hand, the shorter persistency of the instability in OPA most certainly reveals some sensitivity to spurious diapycnal mixing of density despite the relatively low value of the diffusivity coefficient. In absence of spurious mixing, large scale density gradients in MICOM-ADIAB are better preserved, therefore maintaining a higher level of APE storage and allowing more persistent energy production.

In the non-linear phase of the instability, the magnitude of the eddy heat fluxes may be dependent on the timing of the eddy cut-off process which controls the size of the mesoscale features ultimately transporting heat (Drijfhout, 1992). This process should be sensitive to spurious diapycnal mixing of potential vorticity which in  $z$ -coordinate models allows meanders to reach larger amplitude before breaking, possibly leading to an overshoot in the heat flux. Such effects are not identified when comparing the OPA and MICOM-ADIAB simulations which reveal fairly similar eddy size. Differences are however found in the heat flux distribution which cannot be directly attributed to the contrasted distributions of the kinetic energies. In particular, except for a short period between day 5 and day 10, the larger level of eddy kinetic energy in OPA in the first 60 days does not produce higher eddy heat fluxes. Over most of the instability period, better correlation between the eddy velocity field and the density field in MICOM-ADIAB, most probably through a better representation of the vortex stretching distribution which controls the baroclinic energy production, maintains larger, more persistent eddy heat fluxes (see the persistent positive signal between day 40 and 70 in the 0–100 km region in Fig. 16a which is not seen in Fig. 16b). The time evolution of the heat flux is consistent with that of the buoyancy of the convective patch: initially larger in OPA the buoyancy becomes similar or smaller than in MICOM-ADIAB after 40 days.

In both OPA and MICOM-ADIAB, the time scales (as approximated by the e-folding time) of the surface capping of the convective patch and the outward spreading of the cold dense water are roughly similar (Section 3.3). Still, a more detailed comparison of the evolution of the radial distributions of the eddy fluxes (Fig. 15) and eddy kinetic energy (Fig. 9) reveals a larger persistency of the eddy heat fluxes in MICOM-ADIAB which is associated with the spreading of the dense water at depth. The distinct signal in the heat flux reaches its maximum between day 40 and 50, that is with some delay compared to the earlier surface maximum or to the more vertically uniform signal in OPA (Fig. 10). This result is

consistent with observations in convective regions showing a faster surface capping compared to the dense water spreading (Send et al., 1995; Lilly et al., 1999, 2003).

The restratification time scale, as estimated from the evolution of the buoyancy of the convective patch, is only slightly shorter in the  $z$ -model than in the isopycnic model (70 days versus 80 days) leading to fairly similar efficiency coefficients (0.047 versus 0.040). Taking MICOM-ADIAB as the more realistic simulation, we can estimate that about 80% of the initial dense water volume has spread away from the convective patch in 60 days. During that period the buoyancy in the patch increases almost linearly while afterwards, the increase slows down as the isopycnal gradients are progressively eroded. Based on this linear rate, the whole of the convected water would be exported in 75 days, which is very close to the flushing time which can be deduced from Khatiwala and Visbeck (2000) estimate based on observations in the Labrador Sea. These authors calculated a “flushing time”  $\tau_f \approx 3.2$  years, which is the time necessary for a dense layer of thickness  $H = 1000$  m and radius  $R = 200$  km to spread away from the convective patch. Considering that, in our simulations, the dense water initially occupies a layer of thickness 580 m and radius 70 km, a simple proportional relationship to Khatiwala and Visbeck (2000) estimate would give a flushing time  $\tau_f \approx 80$  days. This value is very close to the time scale estimated from the buoyancy change and suggests that, despite the highly idealized stratification in our simulations, the model dynamics in MICOM-ADIAB would be able to reproduce the basic kinetics of the ventilation of the Labrador Sea Water.

In MICOM-ADIAB, the layer physics leads to a strong baroclinicity of the eddies and the associated heat transports. In OPA, the more barotropic structure of the eddies leads to more vertically uniform heat exchanges but, still, those are more intense at intermediate depth than at the surface, contrasting with the surface intensified structure of the kinetic energy. The vertical heat transfers associated with this eddy structure contribute to reestablish some baroclinicity by adding some surface warming and some deeper cooling. Yet this vertical redistribution has a limited effect on the stratification compared with the horizontal contributions. In MICOM, spurious features arise as the bulk of the adiabatic heat transport is constrained to accommodate the geometry of the mixed layer base in order to follow the thickness (or alternatively potential vorticity) gradients. Advection of surrounding water into the convective area therefore mainly occurs underneath the ML, but the reconstitution of the intermediate waters is greatly limited by hydrostatic instability which mixes these waters properties with those of the ML water. Although including a surface buoyancy source would certainly limit these processes through a control of the ML geometry, the associated reverse system of restratification/spreading, in which the dense water initially stored in the deep ML is advected outward at the surface rather than at depth, would still exist. Additionally, that the timing of the restratification be entirely controlled by the atmospheric buoyancy flux is not what is observed in the real ocean.

The predominance of anti-cyclonic eddies as observed in MICOM-ADIAB but not in OPA has been widely observed in the ocean. Based on observations carried out in the Labrador Sea, Lilly et al. (2003) attributed this asymmetry to different evolution of the two eddy categories rather than to different formation processes. This idea is supported by evidence from modeling studies that anti-cyclonic eddies are more stable (Arai and Yamagata, 1994). Yet the asymmetry was not reproduced in an eddy resolving simulation of the restratification period in the Labrador Sea performed with a sigma-coordinate model (Lilly et al., 2003). This would suggest that isopycnic formulation is needed in order to represent the contrasted behavior of cyclonic and anti-cyclonic eddies. On the other hand, eddies appear to have comparable size in OPA and

MICOM-ADIAB. Some comparative studies of the hydrodynamic instabilities in a  $z$ -coordinate model and an isopycnic model forced by wind stress have revealed a smaller sensitivity to lateral dissipation in the isopycnic model (Bleck and Boudra, 1986). Since dissipation in the latter study was parameterized by a scale selective biharmonic operator, these results suggest that the size of the eddies should be larger in the isopycnic model than in the  $z$ -coordinate model. Identifying such differences in our simulations would require a detailed examination of the eddy characteristics which is beyond the scope of this study.

## 5. Summary and concluding remarks

To investigate the impact of different model behavior associated with the representation of the vertical coordinate on the restratification of a deep convective basin, a case study has been analyzed in simulations performed with three different models: a  $z$ -coordinate model, an isopycnic model including a ML, and a “purely isopycnic” model.

The baroclinic conversion of potential energy is the main source of eddy kinetic energy in all simulations. Both the  $z$ -coordinate model and the purely isopycnic model have many features in common. Global indicators like the restratification time scale and the associated instability efficiency are very similar. Still different spatial distributions and time evolutions of both the eddy kinetic energy and the eddy heat fluxes have been identified. At the beginning of the restratification period, the eddy instability grows faster in the  $z$ -coordinate simulation and the kinetic energy reaches a maximum after about 4 weeks. The energy conversion is however less persistent than in the purely adiabatic version of the isopycnic model where the peak value of the kinetic energy is not reached before 6 weeks. It is found that these differences are inherent to the different model physics, and likely to be related to spurious generation of potential vorticity and spurious diapycnal mixing in the  $z$ -coordinate model, which altogether amplify the instability of the rim current in the early stage of the instability and contribute to a decrease of the potential energy available for baroclinic conversion in the later stage. The larger persistence of the instability in the isopycnic model is associated with more persistent lateral heat exchanges at depth in relation to deep water spreading.

Contrasted dynamics exist in the purely isopycnic model, between the upper and dense layers. Warm anti-cyclonic as well as cold cyclonic eddies contribute altogether to the overall warming (resp. cooling) of the upper layers inside (resp. outside) the convective patch. The dense water spreading is essentially achieved by deep cold core anti-cyclones. The time scale of the surface capping and deeper spreading are fairly similar although the latter is more persistent. By contrast, in the  $z$ -coordinate model, heat is predominantly transported by cold core cyclonic eddies with a more barotropic structure. Spreading of dense water with unaltered characteristics is hardly identified. Rather, an overproduction of intermediate water occurs through diapycnal exchanges across the density front surrounding the dense water patch. The warming signal is transported faster inward than the cooling signal is outward.

In the isopycnic model including a ML, the geometry of the ML and the absence of a continuous buoyancy source prevent any retreat of the deep ML in the convective patch. Inclusion of a mixed layer also leads to a weak eddy field with the smaller kinetic energy level among the three simulations. Part of these deficiencies would be certainly avoided by allowing vertical shear in the mixed layer like in the Hallberg isopycnic model (HIM, Hallberg and Rhines, 1996; Thompson et al.,

2002) or by using a hybrid isopycnic-Cartesian coordinates ocean model like HYCOM (Bleck, 2002; Chassignet et al., 2003) in which the discretization of the ML in z-coordinate would greatly improve the physics of the upper layer.

Our analysis neglects the latitudinal dependency of the Coriolis parameter. According to the linear theory of baroclinic instability, this dependency should have a stabilizing effect on the flow field. It should also induce some westward displacement of the convective patch, altering its azimuthal symmetry and therefore the distribution of the lateral exchanges with the surroundings.

## Acknowledgements

We thank Alain Colin de Verdière, Christophe Herbaut, Patrice Klein, Gurvan Madec, Laurent Mortier, and Anne-Marie Tréguier for fruitful discussions about the content of this paper, and Julie Leloup for figures improvements. The authors also thank the two anonymous reviewers for their careful reading and help in improving the manuscript. This work has been supported by the European FP6 project DYNAMITE (contract 003903-GOCE), and by the French project LIVINGSTONE (contract BLAN-NT05-2.43280, funded by Ecole Nationale Supérieure de Techniques Avancées, ENSTA). Computational resources have been provided by the French Institut du Développement et des Ressources en Informatique Scientifique (IDRIS).

## References

- Arai, M., Yamagata, T., 1994. Asymmetric evolution of eddies in rotating shallow water. *Chaos* 42, 163–175.
- Barnier, B. et al., 2001. On the seasonal variability and eddies in the North Brazil current: insights from model intercomparison experiments. *Prog. Oceanogr.* 48, 195–230.
- Bleck, R., 1985. On the conversion between mean and eddy components of potential and kinetic energy in isentropic and isopycnic coordinates. *Dyn. Atmos. Oceans* 9, 17–37.
- Bleck, R., 2002. An oceanic general circulation model framed in hybrid isopycnic-Cartesian coordinates. *Ocean Modell.* 4, 55–58.
- Bleck, R., Boudra, D., 1986. Wind-driven spin-up in eddy-resolving ocean models formulated in isopycnic and isobaric coordinates. *J. Geophys. Res.* 91, 7611–7621.
- Bleck, R., Hu, D., Hanson, H.P., Kraust, E.B., 1989. Mixed layer-thermocline interaction in a three-dimensional isopycnic coordinate model. *J. Phys. Oceanogr.* 19, 1417–1439.
- Bleck, R., Rooth, C., Hu, D., Smith, L.T., 1992. Salinity-driven thermohaline transients in a wind- and thermohaline-forced isopycnic coordinate model of the North Atlantic. *J. Phys. Oceanogr.* 22, 1486–1505.
- Boccaletti, G., Ferrari, R., Fox-Kemper, B., 2007. Mixed layer instabilities and restratification. *J. Phys. Oceanogr.* 35, 1263–1278.
- Chassignet, E.P., Smith, L.T., Halliwell, G.R., Bleck, R., 2003. North Atlantic simulation with the HYbrid Coordinate Ocean Model (HYCOM): Impact of the vertical coordinate choice reference, density, and thermobaricity. *J. Phys. Oceanogr.* 33, 2504–2526.
- Eldevik, T., 2002. On frontal dynamics in two model oceans. *J. Phys. Oceanogr.* 32, 2915–2925.
- Drijfhout, S.S., 1992. Ring genesis and the related heat transport. Part II: a model comparison. *J. Phys. Oceanogr.* 22, 268–285.
- Griffies, S.M. et al., 2000a. Developments in ocean climate modelling. *Ocean Modell.* 2, 123–192.
- Griffies, S.M., Pacanowski, R.C., Hallberg, R.W., 2000b. Spurious diapycnal mixing associated with advection in a z-coordinate ocean model. *Mon. Weather Rev.* 128, 538–564.
- Griffiths, C., Ikeda, M., Smith, P.C., 2000. A numerical model comparison of baroclinic instability in the presence of topography. *Tellus A* 52 (1), 42–65.
- Hallberg, R., Rhines, P., 1996. Buoyancy-driven circulation in an ocean basin with isopycnals intersecting the sloping boundary. *J. Phys. Oceanogr.* 26, 913–940.
- Houssais, M.-N., 1984. Available potential energy for the tourbillon eddy: a tentative energy budget from the CTD mesoscale arrays. *J. Phys. Oceanogr.* 14, 1350–1364.
- Ikeda, M., Wood, R.A., 1993. Mesoscale stability of an ocean current in the Bryan-Cox model. *J. Geophys. Res.* 98, 12527–12536.
- Jones, H., Marshall, J., 1997. Restratification after deep convection. *J. Phys. Oceanogr.* 27, 2276–2287.
- Katsman, C.A., Spall, M.A., Pickart, R.S., 2004. Boundary current eddies and their role in the restratification of the Labrador Sea. *J. Phys. Oceanogr.* 34, 1967–1983.
- Khatiwala, S.P., Visbeck, M., 2000. An estimate of the eddy-induced circulation in the Labrador Sea. *Geophys. Res. Lett.* 27, 2277–2280.
- Kraus, E.B., Turner, J.S., 1967. A one-dimensional model of the seasonal thermocline, II, the general theory and its consequences. *Tellus* 19, 98–105.
- Lilly, J.M. et al., 1999. Observing deep convection in the Labrador Sea during winter 1994/95. *J. Phys. Oceanogr.* 29, 2065–2098.
- Lilly, J.M. et al., 2003. Observations of the Labrador Sea eddy field. *Prog. Oceanogr.* 59, 75–176.
- Lorentz, E., 1967. The Nature and Theory of the General Circulation of the Atmosphere. World Met. Org. Genève.
- Madec, G., Delecluse, P., Crepon, M., Chartier, M., 1991. A three-dimensional numerical study of deep-water formation in the Northwestern Mediterranean Sea. *J. Phys. Oceanogr.* 21, 1349–1371.
- Madec, G., Delecluse, P., Imbard, M., Lévy, C., 1998. OPA8.1 Ocean general circulation model reference manual. Notes de l'IPSL, Université P. et M. Curie, B102 T15-E5, 4 place Jussieu, Paris cedex 5, N°11, 91p.
- Marshall, J., Schott, F., 1999. Open-ocean convection: observations, theory and models. *Rev. Geophys.* 37, 1–64.
- Morawitz, W.M.L. et al., 1996. Three-dimensional observations of a deep convective chimney in the Greenland Sea during winter 1988/1989. *J. Phys. Oceanogr.* 26, 2316–2343.
- Oort, A.H., Ascher, S.C., Levitus, S., Peixoto, J.P., 1989. New estimates of the available potential energy in the world ocean. *J. Geophys. Res.* 94 (C3), 3187–3200.
- Pickart, R.S., Spall, M.A., 2007. Impact of Labrador Sea convection on the North Atlantic Meridional overturning circulation. Submitted to *J. Phys. Oceanogr.*
- Send, U., Schott, F., Gaillard, F., Desaubies, Y., 1995. Observation of a deep convection regime with acoustic tomography. *J. Geophys. Res.* 100 (C4), 6927–6941.
- Smagorinsky, J., 1963. General circulation experiments with the primitive equations. *Mon. Weather Rev.* 91, 99–164.
- Spall, M.A., Chapman, D.C., 1998. On the efficiency of baroclinic eddy heat transport across narrow fronts. *J. Phys. Oceanogr.* 28, 2275–2287.
- Thompson, L., Kelly, K.A., Darr, D., Hallberg, R., 2002. Buoyancy and mixed-layer effects on the sea surface height response in an isopycnal model of the North Pacific. *J. Phys. Oceanogr.* 32, 3657–3670.
- Visbeck, M., Marshall, J., Jones, H., 1996. Dynamics of isolated convective regions in the ocean. *J. Phys. Oceanogr.* 26, 1721–1734.
- Willebrand, J. et al., 2001. Circulation characteristics in three eddy-permitting models of the North Atlantic. *Prog. Oceanogr.* 48, 123–161.